Department of Electrical Engineering and Automation

Weak-Grid Tolerant Control Methods for Voltage-Source Converters

F. M. Mahafugur Rahman

Aalto University

DOCTORAL DISSERTATIONS

Aalto University publication series
DOCTORAL DISSERTATIONS 71/2021

Weak-Grid Tolerant Control Methods for Voltage-Source Converters

F. M. Mahafugur Rahman

A doctoral dissertation completed for the degree of Doctor of Science (Technology) to be defended, with the permission of the Aalto University School of Electrical Engineering, at a public examination held online on 22 June 2021 at 12.

Aalto University
School of Electrical Engineering
Department of Electrical Engineering and Automation
Electric Drives Group

Supervising professor
Prof. Marko Hinkkanen

Thesis advisor
Dr. Jarno Kukkola

Preliminary examiners
Prof. Yasser Abdel-Rady I. Mohamed, University of Alberta, Edmonton, Canada
Prof. Jorge Solsona, Universidad Nacional del Sur, Bahía Blanca, Argentina

Opponent
Prof. Paolo Mattavelli, University of Padua, Padua, Italy

Aalto University publication series
DOCTORAL DISSERTATIONS 71/2021

ISBN 978-952-64-0386-1 (printed)
ISBN 978-952-64-0387-8 (pdf)
ISSN 1799-4934 (printed)
ISSN 1799-4942 (pdf)
http://urn.fi/URN:ISBN:978-952-64-0387-8

Unigrafia Oy
Helsinki 2021

Finland

NORDIC SWAN ECOLABEL
Printed matter
4041-0619

Aalto University

Abstract

Aalto University, P.O. Box 11000, FI-00076 Aalto www.aalto.fi

Author
F. M. Mahafugur Rahman

Name of the doctoral dissertation
Weak-Grid Tolerant Control Methods for Voltage-Source Converters

Publisher School of Electrical Engineering

Unit Department of Electrical Engineering and Automation

Series Aalto University publication series DOCTORAL DISSERTATIONS 71/2021

Field of research Electrical Power and Energy Engineering

Manuscript submitted 18 March 2021 **Date of the defence** 22 June 2021

Permission for public defence granted (date) 3 May 2021 **Language** English

☐ **Monograph** ☒ **Article dissertation** ☐ **Essay dissertation**

Abstract

This thesis deals with weak-grid tolerant control methods for voltage-source converters. The converters suffer from stability problems when connected to weak grids. A grid is categorized as weak if it has a large impedance behind the point of common coupling. In this thesis, two different control methods, state-space current control and power-synchronization control, are studied focusing on weak grids. In the state-space current control, the converter is considered to be equipped with an LCL filter and connected to an inductive grid. The current controller is directly designed in the discrete-time domain. Either the converter or grid current is measured and other states needed by the current controller are estimated using an observer. The closed-form expressions of the discrete-time model are used to design and analyze the current controllers and state observers. The control design is based on the direct pole-placement method with the radial projection for the resonance damping of the LCL filter. The current controller provides good dynamic performance and robust operation against grid strength variations. Furthermore, the controller enables converter operation in a wide range of sampling frequencies. For unbalanced grid operations, the state-space controller is extended to double-frequency current control, during which both positive and negative sequences of the current can be simultaneously controlled. In the power-synchronization control, the converter is considered to be equipped with an L filter and the controller is designed in the continuous-time domain. The power-synchronization control allows robust stability irrespective of the grid strength and of the operating point. Robustness is obtained by analytic gain selections, whereby adequate stability margins are obtained. An enhancement of the power-synchronization control is realized by adding a reference feedforward of the active power, by which a fast dynamic performance can be achieved without step-response ringing and overshoot. Both the state-space current control and power-synchronization control are experimentally evaluated using a 12.5-kVA 50-Hz grid-connected converter. The control methods can be applied in industrial applications, for example, in solar PV and wind turbine systems, as well as the active front-ends of motor drives.

Keywords Disturbance observer, double-frequency controller, full-order observer, grid-connected converter, integrator, L filter, LCL filter, power-synchronization control, reduced-order observer, robustness, state-space current control, voltage-source converter, weak grid

ISBN (printed) 978-952-64-0386-1 **ISBN (pdf)** 978-952-64-0387-8

ISSN (printed) 1799-4934 **ISSN (pdf)** 1799-4942

Location of publisher Helsinki **Location of printing** Helsinki **Year** 2021

Pages 128 **urn** http://urn.fi/URN:ISBN:978-952-64-0387-8

Preface

This research work has been carried out in the Electric Drives research group at the Department of Electrical Engineering and Automation, Aalto University, Finland. This work has been financed in part by ABB Oy, Helsinki, Finland, and in part by MARICI Finland Oy, Helsinki, Finland. The research grants awarded by the Walter Ahlström Foundation and Finnish Foundation for Technology Promotion are gratefully acknowledged.

First of all, I would like to thank Almighty Allah for giving me the opportunity, knowledge, and strength to pursue this research. I am very grateful to my supervisor Prof. Marko Hinkkanen for his guidance and support during my doctoral studies. Prof. Hinkkanen has always been an invaluable mentor throughout my research work. My gratitude also goes to my thesis adviser Dr. Jarno Kukkola, who always encouraged and guided me on this journey. The collaborations with Mr. Ville Pirsto and Dr. Mikko Routimo were really helpful and I wish to thank them for their cooperation.

I would like to thank Adj. Prof. Lennart Harnefors, Prof. Jesús Doval-Gandoy, Dr. Lidong Zhang, and Dr. Diego Pérez-Estévez for their collaboration in the written publications. I wish to express my thanks to all my former and present colleagues as well as the department staff for providing an amazing working environment. I would like to thank the people working at ABB for their constructive and valuable comments on the research work. I would also like to thank all of my Bangladeshi friends residing in Finland for making my life easy here and giving me mental support during the difficult times.

Finally, I would like to express my warmest gratitude to my beloved wife, my brother and sister, and especially to my parents for their endless support throughout my life. Loads of love for you. I dedicate this thesis to my parents.

Espoo, May 10, 2021,

F. M. Mahafugur Rahman

Contents

List of Publications

This thesis consists of an overview and of the following publications which are referred to in the text by their Roman numerals.

I F. M. M. Rahman, U. Riaz, J. Kukkola, M. Routimo, and M. Hinkkanen. Observer-based current control for converters with an LCL filter: Robust design for weak grids. In *Proc. IEEE International Symposium on Sensorless Control for Electrical Drives (SLED)*, Helsinki, Finland, pp. 36-41, September 2018.

II F. M. M. Rahman, V. Pirsto, J. Kukkola, M. Routimo, and M. Hinkkanen. State-space control for LCL filters: Converter versus grid current measurement. *IEEE Transactions on Industry Applications*, vol. 56, no. 6, pp. 6608-6618, November-December 2020.

III F. M. M. Rahman, V. Pirsto, J. Kukkola, M. Hinkkanen, D. Pérez-Estévez, and J. Doval-Gandoy. Equivalence of the integrator-based and disturbance-observer-based state-space current controllers for grid converters. *IEEE Transactions on Industrial Electronics*, vol. 68, no. 6, pp. 4966-4976, June 2021.

IV F. M. M. Rahman, J. Kukkola, V. Pirsto, M. Routimo, and M. Hinkkanen. Observers for discrete-time current control of converters equipped with an LCL filter. In *Proc. IEEE Energy Conversion Congress and Exposition (ECCE)*, Detroit, MI, USA, pp. 2884-2891, October 2020.

V L. Harnefors, M. Hinkkanen, U. Riaz, F. M. M. Rahman, and L. Zhang. Robust analytic design of power-synchronization control. *IEEE Transactions on Industrial Electronics*, vol. 66, no. 8, pp. 5810-5819, August 2019.

VI L. Harnefors, F. M. M. Rahman, M. Hinkkanen, and M. Routimo. Reference-feedforward power-synchronization control. *IEEE Transactions on Power Electronics*, vol. 35, no. 9, pp. 8878-8881, September 2020.

Author's Contribution

Publication I: "Observer-based current control for converters with an LCL filter: Robust design for weak grids"

The author wrote the paper under the guidance of Prof. Hinkkanen. Mr. Riaz contributed by helping with the measurements. Dr. Kukkola and Dr. Routimo contributed by commenting on the manuscript.

Publication II: "State-space control for LCL filters: Converter versus grid current measurement"

The author wrote the paper under the guidance of Dr. Kukkola and Prof. Hinkkanen. Mr. Pirsto contributed by helping with the experiments and participating in the writing of the manuscript. Dr. Routimo contributed by commenting on the manuscript.

Publication III: "Equivalence of the integrator-based and disturbance-observer-based state-space current controllers for grid converters"

The author wrote the paper under the guidance of Dr. Kukkola and Prof. Hinkkanen. Mr. Pirsto contributed to deriving the conditions for the mathematical equivalence of the controllers. Mr. Pirsto also helped with the experiments and participated in the writing of the manuscript. Dr. Pérez-Estévez and Prof. Doval-Gandoy contributed by commenting on the manuscript.

Publication IV: "Observers for discrete-time current control of converters equipped with an LCL filter"

The author wrote the paper under the guidance of Dr. Kukkola and Prof. Hinkkanen. Mr. Pirsto contributed by helping with the experiments and Dr. Routimo by commenting on the manuscript.

Publication V: "Robust analytic design of power-synchronization control"

The author performed the robustness analysis by means of simulations, carried out the experiments, and participated in the writing of the manuscript.

Publication VI: "Reference-feedforward power-synchronization control"

The author performed the experiments and participated in the writing of the manuscript.

Abbreviations

2DOF	Two-degrees-of-freedom
AC	Alternating current
DC	Direct current
DPGS	Distributed power generation system
DSRF	Double synchronous reference frame
LCL	Inductor-capacitor-inductor (filter)
PCC	Point of common coupling
PI	Proportional integral
PLL	Phase-locked loop
PR	Proportional resonant
PSC	Power-synchronization control
PSL	Power-synchronization loop
PWM	Pulse-width modulation
SCR	Short-circuit ratio
VCC	Vector current control
VSC	Voltage-source converter
ZOH	Zero-order hold

Symbols

Complex-valued quantities are marked with boldface italic symbols, vectors with bold-face lowercase symbols, and matrices with boldface upper-case symbols. Vectors in stationary coordinates are marked with superscript s and state estimates with a hat. Reference values are marked with subscript ref, and limited reference values with overline. Subscript + is used for positive-sequence components and subscript – for negative-sequence components.

$\mathbf{A}_\mathrm{p}, \mathbf{B}_\mathrm{c}, \mathbf{B}_\mathrm{g}$	Continuous-time system matrices
C_dc	DC-link capacitance
C_f	LCL-filter capacitance
$\mathbf{C}_\mathrm{g}$	Output vector for the grid current
$\boldsymbol{e}_\mathrm{g}$	Grid voltage
E_g	Grid voltage magnitude
f_s	Sampling frequency
$\mathbf{I}$	Identity matrix
$\boldsymbol{i}_\mathrm{c}$	Converter current
$\boldsymbol{i}_\mathrm{c,f}$	Low-pass filtered converter current
$\boldsymbol{i}_\mathrm{g}$	Grid current
$i_\mathrm{gd}, i_\mathrm{gq}$	Real and imaginary components of $\boldsymbol{i}_\mathrm{g}$
j	Imaginary unit
k	Discrete-time index
$\mathbf{K}_\mathrm{fi}, \mathbf{K}_\mathrm{fd}$	Controller state-feedback gains
$\boldsymbol{k}_\mathrm{c}, \boldsymbol{k}_\mathrm{f}, \boldsymbol{k}_\mathrm{i}, \boldsymbol{k}_\mathrm{t}$	Controller gains

K_d	DC-link voltage control gain
$\mathbf{K}_\mathrm{o}, \mathbf{K}_\mathrm{od}, \boldsymbol{k}_\mathrm{w}$	Observer gains
K_p	Active-power control gain
L_f	Inductance of an L filter
L_fc	Converter-side inductance of an LCL filter
L_fg	Grid-side inductance of an LCL filter
L_g	Grid inductance
P	Active power of the converter
P_dc	External DC-source power
R_a	Active resistance
R_f	Resistance of an L filter
T_s	Sampling period
$\boldsymbol{u}_\mathrm{c}$	Converter voltage
u_dc	DC-link voltage
$\boldsymbol{u}_\mathrm{g}$	PCC voltage
u_g	PCC-voltage magnitude
W	DC-link capacitor energy
$\mathbf{x}, \mathbf{x}_\mathrm{p}, \mathbf{x}_\mathrm{r}$	State vectors
$\boldsymbol{x}_\mathrm{i}$	Integral state
$\boldsymbol{Y}_\mathrm{c}, \boldsymbol{Y}_\mathrm{g}$	Open-loop transfer functions
$\boldsymbol{\Phi}, \boldsymbol{\Gamma}_\mathrm{c}, \boldsymbol{\Gamma}_\mathrm{g}$	Discrete-time system matrices including a delay
$\boldsymbol{\Phi}_\mathrm{p}, \boldsymbol{\Gamma}_\mathrm{cp}, \boldsymbol{\Gamma}_\mathrm{gp}$	Discrete-time system matrices without a delay
ϑ_g	PCC-voltage angle
θ_p	Power-synchronization angle
ω_b	Bandwidth of a low-pass filter
ω_g	Angular frequency of the grid voltage
ω_r	Angular resonance frequency of an LCL filter

1. Introduction

This chapter provides the background for the thesis and reviews previous research related to the topic. It also presents the main objectives and structure of the thesis.

1.1 Background

Voltage-source converters (VSCs) are increasingly used to integrate distributed and renewable energy sources, such as solar photovoltaic (PV) and wind energy systems, into the electric grid. Distributed power generation systems (DPGSs) provide a few advantages including less transmission and distribution losses, improved regulation of local voltages, and enhanced local reliability as compared to a conventional centralized electric power generation system. However, the complexity of the overall electric power system increases with the rising penetration of DPGSs into the grid. The electric grid becomes more difficult to control due to converter-converter and converter-grid interactions (Enslin and Heskes, 2004; Agorreta et al., 2011; Cavazzana et al., 2016; Song et al., 2017). Therefore, suitable control methods for the VSCs are required for reliable and stable operation of the grid-connected system.

The DPGSs are often located in remote areas, which typically are far away from the load centers. The connection of DPGSs to the grid may require long transmission lines, resulting in large grid impedance seen from the point of common coupling (PCC). The grid impedance is related to the short-circuit ratio (SCR), which is the ratio of the short-circuit capacity of the AC system to the rated DC power of a converter (IEEE Std. 1204-1997). The strength of the grid is typically determined using the SCR. The grid is categorized as strong when SCR > 3, weak when 2 < SCR < 3, and very weak if SCR < 2 (Egea-Alvarez et al., 2015; Mortazavian and Mohamed, 2018). When DPGSs are connected to a weak grid, the large and unknown grid impedance may lead to unstable operation of the converter (Liserre et al., 2006; Strachan and Jovcic, 2010; Zhou et al.,

2014; Egea-Alvarez et al., 2015; Arani and Mohamed, 2017). However, converter systems should preferably be capable to operate in weak grids. Therefore, the effects of the grid impedance must be considered when designing control methods for converters.

A low-pass power filter is often inserted between the VSC and the utility grid to attenuate the switching harmonics generated by the pulse width modulator (PWM). An LCL filter is mostly used because of its compact size and better grid current quality in comparison with an L filter (Liserre et al., 2005; Jalili and Bernet, 2009). However, the LCL filter presents a resonant behavior that needs to be damped. The resonance can be damped actively or passively. Active resonance damping of the LCL filter by means of a control, for example, presented by Gabe et al. (2009), Tang et al. (2012), and Wang et al. (2016b), improves the system efficiency as compared to passive damping (Liserre et al., 2005; Peña-Alzola et al., 2013). However, the active damping can be challenging due to the large grid impedance under weak grid conditions (Liserre et al., 2006; Pan et al., 2014).

Vector current control (VCC) is the most popular control method used for grid-connected VSCs. The most commonly used techniques for VCC are proportional-integral (PI) control (Zmood et al., 2001; Liserre et al., 2005; Dannehl et al., 2009; Hwang et al., 2010), proportional-resonant (PR) control (Zmood et al., 2001; Zmood and Holmes, 2003; Liserre et al., 2006; Hwang et al., 2010), and state-space control (Gabe et al., 2009; Dannehl et al., 2010b; Miskovic et al., 2014; Kukkola et al., 2015; Busada et al., 2015; Pérez-Estévez et al., 2018). If the VSCs are connected to weak grids, the potential of the VSCs may not be fully utilized with conventional VCCs (Durrant et al., 2003; Zhou et al., 2014; Egea-Alvarez et al., 2015). Without PCC voltage support, the VCC can not transmit the active power of 1 p.u. to the grid if the SCR = 1. The weak grid may cause low-frequency stability problems due to the coupling between the converter dynamics and the grid dynamics (Harnefors et al., 2007; Messo et al., 2013; Dong et al., 2015; Huang et al., 2016). For example, the phase-locked loop (PLL) dynamics interact with the current control dynamics, thereby resulting in a negative impact on the control performance of the VSCs in weak grids (Harnefors et al., 2007; Zhou and Gole, 2012; Zhou et al., 2014).

A time delay (due to sampling, PWM, and computation) in the current-control loop affects the system stability, particularly if an LCL filter is used. Due to the delay, the stability of single-loop PI or PR control depends on the ratio between the resonance frequency of the system and the sampling frequency (Dannehl et al., 2009; Parker et al., 2014; Zou et al., 2014). For example, a single-loop grid-current PI control is unstable if the resonance frequency of the system is below one sixth of the sampling frequency (Wang et al., 2016a; Xin et al., 2017). In contrast, state-space control can stabilize the system independently of the resonance frequency, as demonstrated by Pérez-Estévez et al. (2017). Furthermore, unlike PI or PR control, for

example, presented by Tang et al. (2012), Agorreta et al. (2011), Dannehl et al. (2010a), and Wang et al. (2016b), no additional damping mechanism is needed in state-space control.

State-space control offers a flexible framework for setting the dominant dynamics of the closed-loop system. In the case of the LCL filter, all the states can either be measured (Wu and Lehn, 2006; Dannehl et al., 2010b; Khajehoddin et al., 2018; Rodríguez-Cabero et al., 2019) or estimated using an observer (Huerta et al., 2012; Kukkola et al., 2015; Tran et al., 2018; Huerta et al., 2018; Bimarta and Kim, 2020). The use of an observer increases reliability, reduces the number of sensors, and decreases the costs in comparison with the current control in which all the states are measured. In state-space control, the controller gains can be solved, for example, by using the system parameters and the desired pole locations, as presented by Dannehl et al. (2010b) and Kukkola et al. (2015). However, the actual poles of the system, which determine the control bandwidth, depend on the unknown grid impedance. In the literature, either the grid impedance has not been considered (Dannehl et al., 2010b; Miskovic et al., 2014; Busada et al., 2015) or the effects of the grid impedance on the stability have only been analyzed for SCR > 3 (Xue et al., 2012; Kukkola et al., 2015; Pérez-Estévez et al., 2017). This thesis focuses on the observer-based state-space current control, particularly with challenging conditions in very weak grids.

Power-synchronization control (PSC) provides superior performance for VSCs connected to weak grids as compared to conventional VCCs (Zhang et al., 2010; Zhang, 2010; Fu et al., 2016). A major feature of the PSC is that a PLL does not have to be used, at least not during normal operation. In PSC, the VSC synchronizes with the grid through an active-power control loop (Alawasa and Mohamed, 2015; Radwan and Mohamed, 2016). The selection of the gain for the active-power control is critical for obtaining satisfactory performance in terms of bandwidth and robustness against grid strength. The gain selection can be decided based on a trial-and-error method, which is typically undesirable. In this approach, the closed-loop system may not guarantee adequate stability margins (Zhang et al., 2011a; Radwan and Mohamed, 2016). A research challenge is to design the PSC in such a way that it does not require a trial-and-error method in the control tuning. The proposed design should ensure a robust stability irrespective of the grid strength and of the operating point.

1.2 Objective and Outline of the Thesis

The objective of this thesis is to develop control methods for grid-connected VSCs with the following properties:

- The control methods should provide a good dynamic performance.

- The proposed control designs should be robust against grid strength variations, ranging from strong to very weak grid conditions. The proposed designs should provide robust operation without changing the tuning of the control system.
- The proposed methods should also operate with large errors in the filter parameters.

This thesis provides control designs for robust operation against grid strength variations for an observer-based state-space current control as well as for PSC. The stability of the controllers is verified by means of analyses and experiments.

This thesis consists of an overview and six publications. The overview is organized as follows. Chapter 2 provides the analytical models and overview of grid converter systems. Chapter 3 reviews the control methods available in the literature and presents state-space control and PSC in detail. Chapter 4 describes the experimental test setup used in the publications. In Chapter 5, the summaries of the publications and the scientific contributions are presented. Chapter 6 concludes the thesis.

2. System Model

This chapter presents theory related to space vectors, an overview of a grid converter, and pulse-width modulation. This chapter also includes the dynamic models of L and LCL filters followed by the grid and DC-link models.

2.1 Space Vectors

A standard three-phase three-wire grid converter system is considered. Since there is no path (no neutral connection) for zero-sequence current to flow, the zero-sequence components are disregarded (Akagi et al., 2007). In order to model the grid converter system, complex space vectors are used throughout the thesis. Vectors are denoted using boldface italic symbols. For example, the space vector of the grid current is $\boldsymbol{i}_{\mathrm{g}}^{\mathrm{s}} = i_{\mathrm{g}\alpha} + \mathrm{j} i_{\mathrm{g}\beta}$, where $i_{\mathrm{g}\alpha}$ and $i_{\mathrm{g}\beta}$ are the orthogonal components of the grid current vector in stationary coordinates. The superscript s is used to denote the stationary reference frame. With peak-value scaling, the space vector of the grid current is defined based on the Clarke transformation as

$$\boldsymbol{i}_{\mathrm{g}}^{\mathrm{s}} = \frac{2}{3}\left(i_{\mathrm{ga}} + \mathrm{e}^{\mathrm{j}2\pi/3} i_{\mathrm{gb}} + \mathrm{e}^{\mathrm{j}4\pi/3} i_{\mathrm{gc}}\right) \tag{2.1}$$

where i_{ga}, i_{gb}, and i_{gc} are the instantaneous phase currents.

The grid current vector $\boldsymbol{i}_{\mathrm{g}}^{\mathrm{s}}$ can be transformed to a synchronous reference frame from the stationary reference frame using the Park transformation as

$$\boldsymbol{i}_{\mathrm{g}} = \boldsymbol{i}_{\mathrm{g}}^{\mathrm{s}} \mathrm{e}^{-\mathrm{j}\vartheta_{\mathrm{g}}} \tag{2.2}$$

where ϑ_{g} is the angle of the synchronous reference frame with respect to the stationary reference frame. The grid current in the synchronous reference frame is $\boldsymbol{i}_{\mathrm{g}} = i_{\mathrm{gd}} + \mathrm{j} i_{\mathrm{gq}}$, where the components of the space vector are denoted by subscripts d and q (no superscript is also used). The AC quantities of three-phase systems become DC-valued components in the steady state in the synchronous reference frame. Hence, designing controllers in the

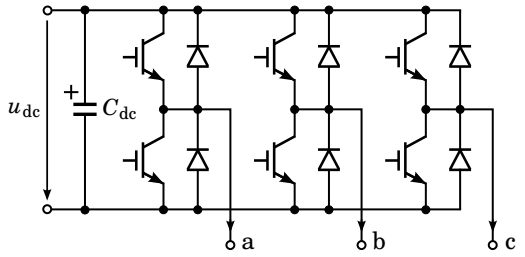

Figure 2.1. Model of a three-phase two-level grid converter.

synchronous reference frame becomes simpler as compared to design in the stationary reference frame.

2.2 Grid Converter

Figure 2.1 shows the model of a three-phase two-level grid converter. The DC-link voltage is denoted by u_{dc} and the DC-link capacitance by C_{dc}. The operation of the converter is based on the PWM technique. In this thesis, the modified suboscillation (also known as symmetrical suboscillation) method for the PWM is used (Holtz, 1994). At every sample instant, the duty ratios $\boldsymbol{d}_{abc} = [d_a, d_b, d_c]^T$ (between 0…1) are calculated using the converter voltage reference $\boldsymbol{u}^s_{c,ref}$ and the DC-link voltage u_{dc}. The gate signals $\boldsymbol{q}_{abc} = [q_a, q_b, q_c]^T$ are obtained by comparing the duty ratios $\boldsymbol{d}_{abc}$ with a carrier signal.

For the dynamic analysis of the system and control design, switching-cycle-averaged voltage is assumed. The average converter voltage space vector over the sampling period T_s is

$$\boldsymbol{u}^s_c = \frac{2}{3}\left(d_a + e^{j2\pi/3} d_b + e^{j4\pi/3} d_c\right) u_{dc}. \tag{2.3}$$

The converter voltage in stationary coordinates is assumed to be piecewise constant between two consecutive sampling instants, which corresponds to the zero-order hold (ZOH) in stator coordinates (Kukkola et al., 2015). In other words, the converter voltage $\boldsymbol{u}^s_c$ is constant during $kT_s < t < (k+1)T_s$, where k is the discrete-time index. It is worth mentioning that the control methods presented in this thesis are compatible with both the single-update PWM (sampling frequency equals the switching frequency) and the double-update PWM (sampling frequency equals twice the switching frequency) (Buso and Mattavelli, 2006).

2.3 Filter

In order to attenuate switching harmonics generated by the PWM and to comply with grid standards such as IEEE Std. 519-2014, a low-pass

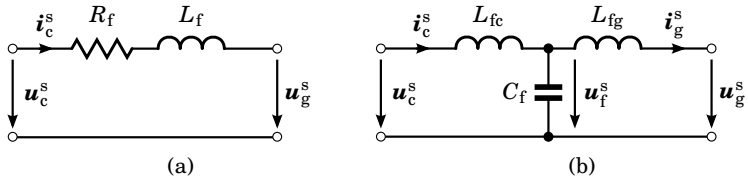

Figure 2.2. Space-vector circuit model in stationary coordinates: (a) L filter; and (b) LCL filter.

power filter is inserted between the converter and the utility grid (Jalili and Bernet, 2009; Beres et al., 2016). An L filter, shown in Figure 2.2(a), is the simplest structure to use. However, it has only 20 dBS per decade attenuation. The most widely used structure is a third-order LCL filter, shown in Figure 2.2(b). The LCL filter provides 60 dBS per decade attenuation for the grid current harmonics at high frequencies (Jiao and Lee, 2015). In order to have the same filtering performance, the total inductance needed in the LCL filter is much smaller than the inductance needed in the L filter (Liserre et al., 2005). However, a disadvantage of the LCL filter is that it presents a resonant behavior. If the resonance of the LCL filter is not damped using an additional damping resistor, it has to be taken into consideration when designing a control method.

2.3.1 L Filter

Figure 2.2(a) shows the space-vector circuit model of the L filter. The converter current is denoted by $\boldsymbol{i}_c^s$ and the voltage at the PCC by $\boldsymbol{u}_g^s$. The filter inductance is L_f and the series resistance is R_f. In this thesis, the filter is assumed to be symmetrical, i.e., the corresponding components for each phase are identical. In the stationary reference frame, the dynamics of the L filter shown in Figure 2.2(a) can be described as

$$L_f \frac{\mathrm{d}\boldsymbol{i}_c^s}{\mathrm{d}t} = \boldsymbol{u}_c^s - R_f \boldsymbol{i}_c^s - \boldsymbol{u}_g^s. \tag{2.4}$$

In synchronous coordinates rotating at the grid angular frequency ω_g, the dynamics of the L filter become

$$L_f \frac{\mathrm{d}\boldsymbol{i}_c}{\mathrm{d}t} + \mathrm{j}\omega_g L_f \boldsymbol{i}_c = \boldsymbol{u}_c - R_f \boldsymbol{i}_c - \boldsymbol{u}_g. \tag{2.5}$$

Transfer functions of the system to be controlled can be derived from (2.5). The transfer function from the converter voltage $\boldsymbol{u}_c$ to the converter current $\boldsymbol{i}_c$ is given by

$$\frac{\boldsymbol{i}_c(s)}{\boldsymbol{u}_c(s)} = \frac{1}{(s + \mathrm{j}\omega_g)L_f + R_f} \tag{2.6}$$

and from the PCC voltage $\boldsymbol{u}_g$ to the converter current $\boldsymbol{i}_c$ by

$$\frac{\boldsymbol{i}_c(s)}{\boldsymbol{u}_g(s)} = -\frac{1}{(s + \mathrm{j}\omega_g)L_f + R_f}. \tag{2.7}$$

For simplicity, the series resistance R_f is often neglected in the analysis and control design.

2.3.2 LCL Filter

Figure 2.2(b) shows the space-vector circuit model of the LCL filter. The converter-side inductance is L_fc, the capacitance is C_f, and the grid-side inductance is L_fg. The voltage across the capacitor is denoted by $\boldsymbol{u}_\mathrm{f}^\mathrm{s}$. The losses due to the resistances in the filter are neglected to simplify the analysis. Moreover, the loss-less filter presents the worst-case scenario for the resonance of the LCL filter. For a three-phase symmetrical system, the dynamics of the LCL filter are described by

$$\begin{aligned} L_\mathrm{fc}\frac{\mathrm{d}\boldsymbol{i}_\mathrm{c}^\mathrm{s}}{\mathrm{d}t} &= \boldsymbol{u}_\mathrm{c}^\mathrm{s} - \boldsymbol{u}_\mathrm{f}^\mathrm{s} \\ C_\mathrm{f}\frac{\mathrm{d}\boldsymbol{u}_\mathrm{f}^\mathrm{s}}{\mathrm{d}t} &= \boldsymbol{i}_\mathrm{c}^\mathrm{s} - \boldsymbol{i}_\mathrm{g}^\mathrm{s} \\ L_\mathrm{fg}\frac{\mathrm{d}\boldsymbol{i}_\mathrm{g}^\mathrm{s}}{\mathrm{d}t} &= \boldsymbol{u}_\mathrm{f}^\mathrm{s} - \boldsymbol{u}_\mathrm{g}^\mathrm{s}. \end{aligned} \tag{2.8}$$

In state-space form, the dynamics of the LCL filter can be represented as

$$\frac{\mathrm{d}\mathbf{x}_\mathrm{p}^\mathrm{s}}{\mathrm{d}t} = \underbrace{\begin{bmatrix} 0 & \frac{1}{L_\mathrm{fg}} & 0 \\ -\frac{1}{C_\mathrm{f}} & 0 & \frac{1}{C_\mathrm{f}} \\ 0 & -\frac{1}{L_\mathrm{fc}} & 0 \end{bmatrix}}_{\mathbf{A}_\mathrm{p}^\mathrm{s}} \mathbf{x}_\mathrm{p}^\mathrm{s} + \underbrace{\begin{bmatrix} 0 \\ 0 \\ \frac{1}{L_\mathrm{fc}} \end{bmatrix}}_{\mathbf{B}_\mathrm{c}} \boldsymbol{u}_\mathrm{c}^\mathrm{s} + \underbrace{\begin{bmatrix} -\frac{1}{L_\mathrm{fg}} \\ 0 \\ 0 \end{bmatrix}}_{\mathbf{B}_\mathrm{g}} \boldsymbol{u}_\mathrm{g}^\mathrm{s} \tag{2.9}$$

where $\mathbf{x}_\mathrm{p}^\mathrm{s} = [\boldsymbol{i}_\mathrm{g}^\mathrm{s}, \boldsymbol{u}_\mathrm{f}^\mathrm{s}, \boldsymbol{i}_\mathrm{c}^\mathrm{s}]^\mathrm{T}$ is the state vector, $\mathbf{A}_\mathrm{p}^\mathrm{s}$ is the system matrix, and $\mathbf{B}_\mathrm{c}$ and $\mathbf{B}_\mathrm{g}$ are the input vectors for the converter and PCC voltages, respectively. In synchronous coordinates rotating at the grid angular frequency ω_g, the dynamics of the LCL filter become

$$\frac{\mathrm{d}\mathbf{x}_\mathrm{p}}{\mathrm{d}t} = \underbrace{\begin{bmatrix} -\mathrm{j}\omega_\mathrm{g} & \frac{1}{L_\mathrm{fg}} & 0 \\ -\frac{1}{C_\mathrm{f}} & -\mathrm{j}\omega_\mathrm{g} & \frac{1}{C_\mathrm{f}} \\ 0 & -\frac{1}{L_\mathrm{fc}} & -\mathrm{j}\omega_\mathrm{g} \end{bmatrix}}_{\mathbf{A}_\mathrm{p}} \mathbf{x}_\mathrm{p} + \underbrace{\begin{bmatrix} 0 \\ 0 \\ \frac{1}{L_\mathrm{fc}} \end{bmatrix}}_{\mathbf{B}_\mathrm{c}} \boldsymbol{u}_\mathrm{c} + \underbrace{\begin{bmatrix} -\frac{1}{L_\mathrm{fg}} \\ 0 \\ 0 \end{bmatrix}}_{\mathbf{B}_\mathrm{g}} \boldsymbol{u}_\mathrm{g}. \tag{2.10}$$

The converter and grid current can be obtained from the state-space representation (2.10), respectively, as

$$\boldsymbol{i}_\mathrm{c} = \underbrace{\begin{bmatrix} 0 & 0 & 1 \end{bmatrix}}_{\mathbf{C}_\mathrm{cp}} \mathbf{x}_\mathrm{p} \quad \text{and} \quad \boldsymbol{i}_\mathrm{g} = \underbrace{\begin{bmatrix} 1 & 0 & 0 \end{bmatrix}}_{\mathbf{C}_\mathrm{gp}} \mathbf{x}_\mathrm{p}. \tag{2.11}$$

The transfer function from the converter voltage to the converter current is given by

$$\frac{\boldsymbol{i}_\mathrm{c}(s)}{\boldsymbol{u}_\mathrm{c}(s)} = \boldsymbol{Y}_\mathrm{cp}(s) = \mathbf{C}_\mathrm{cp}(s\mathbf{I} - \mathbf{A}_\mathrm{p})^{-1}\mathbf{B}_\mathrm{c} = \frac{1}{L_\mathrm{fc}} \frac{(s + \mathrm{j}\omega_\mathrm{g})^2 + \omega_\mathrm{z}^2}{(s + \mathrm{j}\omega_\mathrm{g})\left[(s + \mathrm{j}\omega_\mathrm{g})^2 + \omega_\mathrm{r}^2\right]} \tag{2.12}$$

and the transfer function from the converter voltage to the grid current by

$$\frac{\boldsymbol{i}_{\mathrm{g}}(s)}{\boldsymbol{u}_{\mathrm{c}}(s)} = \boldsymbol{Y}_{\mathrm{gp}}(s) = \mathbf{C}_{\mathrm{gp}}(s\mathbf{I} - \mathbf{A}_{\mathrm{p}})^{-1}\mathbf{B}_{\mathrm{c}} = \frac{1}{L_{\mathrm{fc}}C_{\mathrm{f}}L_{\mathrm{fg}}} \frac{1}{(s + \mathrm{j}\omega_{\mathrm{g}})\left[(s + \mathrm{j}\omega_{\mathrm{g}})^2 + \omega_{\mathrm{r}}^2\right]} \tag{2.13}$$

where $\mathbf{I}$ is the identity matrix and

$$\omega_{\mathrm{r}} = \sqrt{\frac{L_{\mathrm{fc}} + L_{\mathrm{fg}}}{L_{\mathrm{fc}}C_{\mathrm{f}}L_{\mathrm{fg}}}} \quad \text{and} \quad \omega_{\mathrm{z}} = \sqrt{\frac{1}{L_{\mathrm{fg}}C_{\mathrm{f}}}} \tag{2.14}$$

are the resonance and anti-resonance frequencies of the LCL filter, respectively. Other transfer functions can be similarly obtained.

Discrete-Time Model

In Publications I and IV, the controllers are directly designed in the discrete-time domain. Hence, a discrete representation is required of the state-space model (2.10). The following assumptions, considered by Kukkola et al. (2015), are made to obtain an exact hold-equivalent discrete-time model. The PWM is modeled as the ZOH in stationary coordinates and the switching-cycle-averaged converter output voltage is considered. Hence, the converter voltage $\boldsymbol{u}_{\mathrm{c}}^{\mathrm{s}}$ remains constant between two consecutive sampling instants. The measurements, for example, the converter current and grid current, are synchronously sampled with the ZOH. Under these assumptions, the hold-equivalent discrete-time model of (2.10) can be expressed as

$$\mathbf{x}_{\mathrm{p}}(k+1) = \boldsymbol{\Phi}_{\mathrm{p}}\mathbf{x}_{\mathrm{p}}(k) + \boldsymbol{\Gamma}_{\mathrm{cp}}\boldsymbol{u}_{\mathrm{c}}(k) + \boldsymbol{\Gamma}_{\mathrm{gp}}\boldsymbol{u}_{\mathrm{g}}(k) \tag{2.15}$$

where the system matrices $\boldsymbol{\Phi}_{\mathrm{p}}$, $\boldsymbol{\Gamma}_{\mathrm{cp}}$, and $\boldsymbol{\Gamma}_{\mathrm{gp}}$ are obtained from (2.10), as (Kukkola et al., 2015)

$$\boldsymbol{\Phi}_{\mathrm{p}} = \mathrm{e}^{\mathbf{A}_{\mathrm{p}}T_{\mathrm{s}}} = \boldsymbol{\gamma}\begin{bmatrix} \frac{L_{\mathrm{fg}}+L_{\mathrm{fc}}\cos(\omega_{\mathrm{r}}T_{\mathrm{s}})}{L_{\mathrm{fc}}+L_{\mathrm{fg}}} & \frac{\sin(\omega_{\mathrm{r}}T_{\mathrm{s}})}{\omega_{\mathrm{r}}L_{\mathrm{fg}}} & \frac{L_{\mathrm{fc}}[1-\cos(\omega_{\mathrm{r}}T_{\mathrm{s}})]}{L_{\mathrm{fc}}+L_{\mathrm{fg}}} \\ -\frac{\sin(\omega_{\mathrm{r}}T_{\mathrm{s}})}{\omega_{\mathrm{r}}C_{\mathrm{f}}} & \cos(\omega_{\mathrm{r}}T_{\mathrm{s}}) & \frac{\sin(\omega_{\mathrm{r}}T_{\mathrm{s}})}{\omega_{\mathrm{r}}C_{\mathrm{f}}} \\ \frac{L_{\mathrm{fg}}[1-\cos(\omega_{\mathrm{r}}T_{\mathrm{s}})]}{L_{\mathrm{fc}}+L_{\mathrm{fg}}} & -\frac{\sin(\omega_{\mathrm{r}}T_{\mathrm{s}})}{\omega_{\mathrm{r}}L_{\mathrm{fc}}} & \frac{L_{\mathrm{fc}}+L_{\mathrm{fg}}\cos(\omega_{\mathrm{r}}T_{\mathrm{s}})}{L_{\mathrm{fc}}+L_{\mathrm{fg}}} \end{bmatrix}$$

$$\boldsymbol{\Gamma}_{\mathrm{cp}} = \int_0^{T_{\mathrm{s}}} \mathrm{e}^{\mathbf{A}_{\mathrm{p}}\tau}\mathrm{e}^{-\mathrm{j}\omega_{\mathrm{g}}(T_{\mathrm{s}}-\tau)}\mathrm{d}\tau \cdot \mathbf{B}_{\mathrm{c}} = \frac{\boldsymbol{\gamma}}{L_{\mathrm{fc}}+L_{\mathrm{fg}}}\begin{bmatrix} T_{\mathrm{s}} - \frac{\sin(\omega_{\mathrm{r}}T_{\mathrm{s}})}{\omega_{\mathrm{r}}} \\ L_{\mathrm{fg}}[1-\cos(\omega_{\mathrm{r}}T_{\mathrm{s}})] \\ T_{\mathrm{s}} + \frac{L_{\mathrm{fg}}\sin(\omega_{\mathrm{r}}T_{\mathrm{s}})}{\omega_{\mathrm{r}}L_{\mathrm{fc}}} \end{bmatrix} \tag{2.16}$$

$$\boldsymbol{\Gamma}_{\mathrm{gp}} = \int_0^{T_{\mathrm{s}}} \mathrm{e}^{\mathbf{A}_{\mathrm{p}}\tau}\mathrm{d}\tau \cdot \mathbf{B}_{\mathrm{g}} = \boldsymbol{\gamma}\begin{bmatrix} \frac{\omega_{\mathrm{g}}\omega_{\mathrm{r}}L_{\mathrm{fc}}\sin(\omega_{\mathrm{r}}T_{\mathrm{s}}) - \mathrm{j}\delta L_{\mathrm{fg}} - \mathrm{j}\omega_{\mathrm{g}}^2 L_{\mathrm{fc}}\cos(\omega_{\mathrm{r}}T_{\mathrm{s}}) + \mathrm{j}\mathrm{e}^{\mathrm{j}\omega_{\mathrm{g}}T_{\mathrm{s}}}(\delta L_{\mathrm{fg}} + \omega_{\mathrm{g}}^2 L_{\mathrm{fc}})}{\delta\omega_{\mathrm{g}}L_{\mathrm{fg}}(L_{\mathrm{fc}}+L_{\mathrm{fg}})} \\ \frac{\omega_{\mathrm{r}}\cos(\omega_{\mathrm{r}}T_{\mathrm{s}}) + \mathrm{j}\omega_{\mathrm{g}}\sin(\omega_{\mathrm{r}}T_{\mathrm{s}}) - \mathrm{e}^{\mathrm{j}\omega_{\mathrm{g}}T_{\mathrm{s}}}\omega_{\mathrm{r}}}{\delta\omega_{\mathrm{r}}C_{\mathrm{f}}L_{\mathrm{fg}}} \\ \frac{-\omega_{\mathrm{g}}\omega_{\mathrm{r}}\sin(\omega_{\mathrm{r}}T_{\mathrm{s}}) + \mathrm{j}\omega_{\mathrm{g}}^2\cos(\omega_{\mathrm{r}}T_{\mathrm{s}}) - \mathrm{j}\delta - \mathrm{j}\mathrm{e}^{\mathrm{j}\omega_{\mathrm{g}}T_{\mathrm{s}}}\omega_{\mathrm{r}}^2}{\delta\omega_{\mathrm{g}}(L_{\mathrm{fc}}+L_{\mathrm{fg}})} \end{bmatrix}$$

where $\boldsymbol{\gamma} = \mathrm{e}^{-\mathrm{j}\omega_{\mathrm{g}}T_{\mathrm{s}}}$, and $\delta = \omega_{\mathrm{g}}^2 - \omega_{\mathrm{r}}^2$. The system matrices $\boldsymbol{\Phi}_{\mathrm{p}}$, $\boldsymbol{\Gamma}_{\mathrm{cp}}$, and $\boldsymbol{\Gamma}_{\mathrm{gp}}$ could alternatively be numerically computed (Pérez-Estévez et al., 2017).

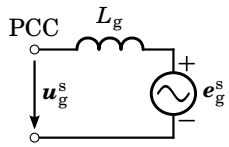

Figure 2.3. Equivalent circuit model of an inductive grid.

2.4 Grid

Figure 2.3 shows a circuit model of an inductive grid. A converter station, consisting of converters and filters, is connected to the grid at the PCC. The converter station could also be connected to the grid through a distribution transformer. Typically, the grid impedance behind the PCC is unknown and time-varying (Jessen et al., 2015). For that reason, exact modeling of the grid is challenging. The grid can be modeled as a voltage source $\boldsymbol{e}_g^s$ or a voltage source with a series-connected inductance L_g, as represented by Kukkola et al. (2015) and Pérez-Estévez et al. (2017). In this thesis, a purely inductive and symmetrical grid is assumed. The inductance L_g shown in Figure 2.3 is the sum of the grid inductance and the inductance of the transformer (if such is used). The grid resistance is omitted in order to reduce the complexity in control design and to simplify the analysis. These approximations of grid model are practical in the control design, as shown in this thesis.

Grid Strength
In this thesis, the grid strength is defined using the SCR, as (Zhang et al., 2011a)

$$\mathrm{SCR} = \frac{1}{L_g\,[\mathrm{p.u.}]}. \tag{2.17}$$

The grid is categorized as strong if SCR > 3 and very weak if SCR < 2 (Egea-Alvarez et al., 2015; Mortazavian and Mohamed, 2018). In (2.17), the SCR is determined using the inductance seen at the PCC. However, to avoid splitting the grid and converter inductances in the case of the L filter, the SCR can be defined as seen from the converter terminals. Similarly, in the case of the LCL filter, the SCR values can be defined at the capacitor terminals of the filter instead of seen from the PCC.

Inclusion of L_g in the Discrete-Time Model
Typically, the controllers are designed with an assumption of a strong grid, for example, with $L_g = 0$, under nominal conditions (Kukkola et al., 2015; Pérez-Estévez et al., 2017). It means that the discrete-time model does not include the grid inductance L_g, thereby $\boldsymbol{u}_g^s = \boldsymbol{e}_g^s$. A similar approach with the assumption $L_g = 0$ is also used in the control designs in Publications I-IV. However, the grid inductance can be taken into account in control tuning if weak grid conditions are to be expected. In Publication II, a very

weak grid assumption (L_g = 1 p.u.) is also used to examine the effect of the grid inductance estimate on the stability of current control. A detailed set of results can be found in Publication II.

If L_g is included in the discrete-time model, the filter inductance L_{fg} needs to be replaced with $L_{fg}+L_g$ in (2.16). It is to be noted that the undamped resonance frequency, obtained using (2.14), depends on the grid inductance L_g, i.e., increasing the grid inductance decreases the resonance frequency of the system.

Grid Voltages

The phase voltages of the grid, oscillating with the angular frequency ω_g and separated by 120° ($2\pi/3$ radians) phase angle, are

$$\begin{aligned} e_{ga} &= E_{ga}\cos\left(\omega_g t + \phi_a\right) \\ e_{gb} &= E_{gb}\cos\left(\omega_g t - 2\pi/3 + \phi_b\right) \\ e_{gc} &= E_{gc}\cos\left(\omega_g t - 4\pi/3 + \phi_c\right) \end{aligned} \tag{2.18}$$

where ϕ_a, ϕ_b, and ϕ_c are the phase shifts. The magnitudes (peak values) of the phase voltages are marked with capital letter. During normal operations, the phase voltages are balanced, i.e., $E_{ga} = E_{gb} = E_{gc} = E_g$ and $\phi_a = \phi_b = \phi_c$, where E_g is the magnitude of the grid voltages. The grid voltage vector $\boldsymbol{e}_g^s$ is defined similarly to (2.1). The magnitude and the rotation speed of the grid voltage vector are constant in the balanced conditions.

During a grid fault, the magnitudes or the phase shifts of the grid phase voltages may be unequal, i.e., $E_{ga} \neq E_{gb} \neq E_{gc}$ or $\phi_a \neq \phi_b \neq \phi_c$, which is typically known as an unbalanced grid. The magnitude and the rotation speed of the grid voltage vector are no longer constant in unbalanced grid conditions. The real grid voltages may also include harmonic components at frequencies multiples of the fundamental frequency (Teodorescu et al., 2011). The harmonics can be similarly modeled with the space vector as the fundamental frequency component. The three-phase waveform corresponding to a positive-sequence space vector (i.e. counterclockwise rotation) is known as a positive-sequence harmonic, and corresponding to a negative-sequence space vector (i.e. clockwise rotation) as a negative-sequence harmonic. The harmonics that are multiples of three (triplen harmonics) are called zero-sequence harmonics (Yazdani and Iravani, 2010).

2.5 DC Link

Figure 2.4 shows an equivalent circuit model of a DC link. An ideal capacitor is considered to model the DC link of the converter. The dynamics of the DC-link voltage are

$$C_{dc}\frac{\mathrm{d}u_{dc}}{\mathrm{d}t} = i_{dc} - i_{in} \tag{2.19}$$

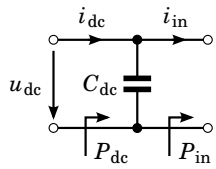

Figure 2.4. Equivalent circuit model of a DC link.

where i_{dc} is the external direct current and i_{in} is the current on the DC side of the semiconductor bridge in the converter. The DC-link dynamics can be expressed in the form of energy stored in the DC link as

$$\frac{dW}{dt} = P_{dc} - P_{in} \tag{2.20}$$

where $W = (1/2)C_{dc}u_{dc}^2$ is the energy stored in the DC-link capacitor, $P_{dc} = u_{dc}i_{dc}$ is the external power supplied into the DC link, and P_{in} is the power on the DC side of the semiconductor bridge in the converter. If the converter losses are neglected, then the input power P_{in} equals the converter output power P.

3. Control Methods

This chapter presents state-space control and power-synchronization control (PSC). The state-space current control is applied to a grid converter equipped with an LCL filter. An observer-based design of state-space control is discussed in detail. Two different structures of state-space control are presented. The PSC is applied to a grid converter equipped with an L filter. Two different schemes of PSC are presented for active-power control. Lastly, DC-link voltage control is discussed.

An overall block diagram is shown first to briefly describe a converter control system. Figure 3.1 shows the typical structure of a current control system for grid converters. The current controller operates in PCC-voltage coordinates, where $\boldsymbol{u}_\mathrm{g} = u_\mathrm{g} + \mathrm{j}0$. The grid current is measured for state-feedback control. The DC-link voltage u_dc is measured for the PWM and the PCC voltage is measured for the PLL. The PCC voltage magnitude is also needed in the AC-voltage controller shown with the dashed line (if such is used). It is worth mentioning that instead of measuring the PCC voltage, control of the converter can be implemented in the estimated PCC-voltage reference frame (Kukkola and Hinkkanen, 2016).

3.1 State-Space Current Control

Various current control methods have been applied to grid converters equipped with an LCL filter. In the literature, PI, PR, and state-space current controllers are the most commonly used. The synchronous-frame PI controller is found to be equivalent to the stationary-frame PR controller (Zmood et al., 2001; Zmood and Holmes, 2003; Hwang et al., 2010). The ratio between the resonance frequency and the sampling frequency affects the stability of single-loop PI or PR current control (Zou et al., 2014; Parker et al., 2014; Wang et al., 2016a,b; Xin et al., 2017). For example, according to Parker et al. (2014), Wang et al. (2016b), and Xin et al. (2017), stability problems arise for the grid current measurement case if the resonance frequency of the system is below one sixth of the sampling frequency. In

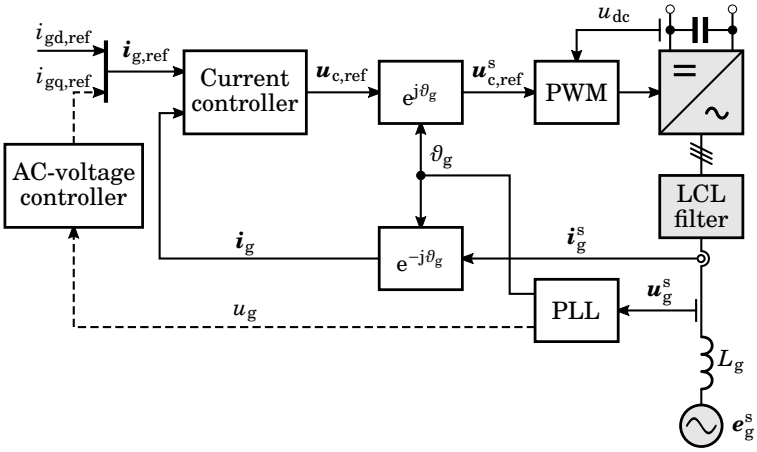

Figure 3.1. Control system of a grid converter in which the current controller is operating in PCC voltage coordinates. The PCC-voltage magnitude u_g and angle ϑ_g are obtained using a PLL. An AC-voltage controller (shown with the dashed line) can be included in the control system.

contrast, state-space control can stabilize the system, independently of the resonance frequency of the filter, as shown by Pérez-Estévez et al. (2017). The state-space current controller has a more complex structure as compared to the conventional PI or PR controller. PI control is merely a special case of state-space control with reference feedforward and integral action. With a suitable selection of controller gains, the state-space controller can be made equivalent to a two-degrees-of-freedom (2DOF) PI controller (Kukkola and Hinkkanen, 2014). The advantage of this modification is valuable in practice. If the state-space control structure has been implemented, the user can easily parametrize it to equal the conventional PI or PR controller without any changes to the implemented structure. Considering these aspects, the state-space structure is used for current control in this thesis.

In state-space control, the closed-loop dynamics can be set through pole-placement methods (Franklin et al., 1997). The closed-loop poles for the desired dynamics can be placed at desired locations, e.g., using direct pole placement (Kukkola and Hinkkanen, 2014; Kukkola et al., 2015; Pérez-Estévez et al., 2017; Pérez-Estévez et al., 2018), linear-quadratic (LQ) control (Busada et al., 2015; Huerta et al., 2018; Khajehoddin et al., 2018; Rodríguez-Cabero et al., 2019; Xie et al., 2020), or H_∞ control (Maccari et al., 2012; Koch et al., 2017, 2019). The direct pole-placement method provides a convenient and straightforward way to solve the controller gains. The gains can be solved analytically (Kukkola and Hinkkanen, 2014; Kukkola et al., 2015) or numerically (Pérez-Estévez et al., 2017) using the system parameters and the desired pole locations. No additional active damping mechanism for the LCL filter is needed in state-space control if properly designed. The direct discrete-time design improves pole-

placement accuracy in the case of low sampling frequencies, resulting in a superior performance and better resonance damping of the system as compared to the continuous-time design, as demonstrated by Turner et al. (2011) and Kukkola et al. (2015). In addition, the intrinsic delay can be easily taken into account in the direct discrete-time design approach (Kukkola et al., 2015; Pérez-Estévez et al., 2017). In this thesis, the state-space current controller is directly designed in the discrete-time domain.

The integral action in state-space control can be implemented in two ways (Franklin et al., 1997): integral control by state augmentation or disturbance estimation using an observer. The integral action is included in the control law in the case of state augmentation, which is called the integrator-based design. In contrast, the integral action is a part of the state observer in the case of disturbance-observer-based design. Both structures have been used for control of grid-connected converters (Kukkola et al., 2015; Pérez-Estévez et al., 2017). This thesis describes both state-space control structures and presents the links between them.

3.1.1 Inclusion of the Control Delay

A computational delay of one sampling period exists in standard implementations (Kukkola et al., 2015; Pérez-Estévez et al., 2017). The computational delay can be easily included in the plant model (2.15). In stationary coordinates, the computational delay is modeled as $\boldsymbol{u}_{\mathrm{c}}^{\mathrm{s}}(k+1) = \boldsymbol{u}_{\mathrm{c,ref}}^{\mathrm{s}}(k)$, where $\boldsymbol{u}_{\mathrm{c,ref}}^{\mathrm{s}}$ is the voltage reference for the PWM, as shown in Figure 3.1. The effect of the computational delay, in synchronous coordinates, can be modeled as

$$\boldsymbol{u}_{\mathrm{c}}(k+1) = \boldsymbol{\gamma}\boldsymbol{u}_{\mathrm{c,ref}}(k) \tag{3.1}$$

where $\boldsymbol{\gamma} = \mathrm{e}^{-\mathrm{j}\omega_{\mathrm{g}}T_{\mathrm{s}}}$. With this delay and considering $L_{\mathrm{g}} = 0$ ($\boldsymbol{u}_{\mathrm{g}}^{\mathrm{s}} = \boldsymbol{e}_{\mathrm{g}}^{\mathrm{s}}$), the discrete-time model of the system can be written as

$$\mathbf{x}(k+1) = \underbrace{\begin{bmatrix} \boldsymbol{\Phi}_{\mathrm{p}} & \boldsymbol{\Gamma}_{\mathrm{cp}} \\ \mathbf{0} & 0 \end{bmatrix}}_{\boldsymbol{\Phi}} \mathbf{x}(k) + \underbrace{\begin{bmatrix} \mathbf{0} \\ \boldsymbol{\gamma} \end{bmatrix}}_{\boldsymbol{\Gamma}_{\mathrm{c}}} \boldsymbol{u}_{\mathrm{c,ref}}(k) + \underbrace{\begin{bmatrix} \boldsymbol{\Gamma}_{\mathrm{gp}} \\ 0 \end{bmatrix}}_{\boldsymbol{\Gamma}_{\mathrm{g}}} \boldsymbol{e}_{\mathrm{g}}(k) \tag{3.2}$$

$$\boldsymbol{i}_{\mathrm{g}}(k) = \underbrace{\begin{bmatrix} 1 & 0 & 0 & 0 \end{bmatrix}}_{\mathbf{C}_{\mathrm{g}}} \mathbf{x}(k) \tag{3.3}$$

where $\mathbf{x} = [\boldsymbol{i}_{\mathrm{g}}, \boldsymbol{u}_{\mathrm{f}}, \boldsymbol{i}_{\mathrm{c}}, \boldsymbol{u}_{\mathrm{c}}]^{\mathrm{T}}$ is the new state vector. Since the computational delay (3.1) is included in the discrete-time model, the order of the system model (3.2) increases by one as compared to the model (2.15). The system model (3.2) together with (3.3) relates the grid current $\boldsymbol{i}_{\mathrm{g}}$ to the converter voltage reference $\boldsymbol{u}_{\mathrm{c,ref}}$ and the grid voltage $\boldsymbol{e}_{\mathrm{g}}$. The model can also be

expressed in the form of transfer functions

$$\boldsymbol{Y}_{\mathrm{c}}(z) = \frac{\boldsymbol{i}_{\mathrm{g}}(z)}{\boldsymbol{u}_{\mathrm{c,ref}}(z)} = \mathbf{C}_{\mathrm{g}}(z\mathbf{I} - \boldsymbol{\Phi})^{-1}\boldsymbol{\Gamma}_{\mathrm{c}} \tag{3.4}$$

$$\boldsymbol{Y}_{\mathrm{g}}(z) = \frac{\boldsymbol{i}_{\mathrm{g}}(z)}{\boldsymbol{e}_{\mathrm{g}}(z)} = \mathbf{C}_{\mathrm{g}}(z\mathbf{I} - \boldsymbol{\Phi})^{-1}\boldsymbol{\Gamma}_{\mathrm{g}}. \tag{3.5}$$

3.1.2 State Observers

In state-space control, all the states in the system must be measured (Dannehl et al., 2010b; Wu and Lehn, 2006; Rodríguez-Cabero et al., 2019; Khajehoddin et al., 2018) or estimated using an observer (Huerta et al., 2012; Tran et al., 2018; Kukkola et al., 2015; Huerta et al., 2018; Bimarta and Kim, 2020). The complexity of the overall control system increases in the case of observer-based design. However, due to less sensors being used in the system, it becomes more reliable and cost-effective as compared to the control system in which all the states are measured.

In the grid converter system shown in Figure 3.1, the control method is based on the grid current measurement. The other states (converter current and voltage across the filter capacitor) can be estimated using either a full-order observer (Kukkola et al., 2015; Huerta et al., 2012; Miskovic et al., 2014; Huerta et al., 2018) or a reduced-order observer (Pérez-Estévez et al., 2017; Su et al., 2019). The full-order observer is the most commonly used structure found in the literature, which reconstructs all the states of the system, i.e., the measured state as well as the unmeasured states. In the discrete-time domain, there are two alternative structures for the full-order observer: the current-type observer and the prediction-type observer (Franklin et al., 1997). In contrast to the full-order observers, the reduced-order observer only reconstructs the unmeasured states.

The discrete-time model (3.2), consisting of the LCL filter and unit delay, is used to design the reduced-order observer presented in Publication III. In this case, the converter voltage is also estimated in addition to the unmeasured states of the plant. The discrete-time model (2.15) (i.e., without including the delay effect) can also be used for the observer design, which means that the converter voltage is excluded from the observer. In Publications I, II, and IV, the delayed voltage reference $\boldsymbol{u}_{\mathrm{c}}(k) = \boldsymbol{\gamma}\boldsymbol{u}_{\mathrm{c,ref}}(k-1)$ is used in the control system instead of using the estimated converter voltage $\hat{\boldsymbol{u}}_{\mathrm{c}}$.

All three different observers, the current-type observer, the prediction-type observer, and the reduced-order observer, are presented for discrete-time state-space current control in Publication IV. The robustness against the grid strength variations is compared, as well as robustness against the errors in the filter parameters, and the dynamic performance obtained with these three observers. In addition, the performance obtained with all three

observers is contrasted with the performance resulting from the control without an observer, i.e., the current control in which all the states are measured. With a suitable selection of the observer gain, the current-type observer is shown to be mathematically equivalent to the reduced-order observer.

Reduced-Order Observer: An Example

The discrete-time model (3.2) is used to design the reduced-order observer. For its design, the state vector $\mathbf{x}$ is split into the measured state $\boldsymbol{i}_\mathrm{g}$ and the states $\mathbf{x}_\mathrm{r} = [\boldsymbol{u}_\mathrm{f}, \boldsymbol{i}_\mathrm{c}, \boldsymbol{u}_\mathrm{c}]^\mathrm{T}$ to be estimated. The system model (3.2) becomes

$$\begin{bmatrix} \boldsymbol{i}_\mathrm{g}(k+1) \\ \mathbf{x}_\mathrm{r}(k+1) \end{bmatrix} = \underbrace{\begin{bmatrix} \boldsymbol{\phi}_\mathrm{aa} & \boldsymbol{\Phi}_\mathrm{ab} \\ \boldsymbol{\Phi}_\mathrm{ba} & \boldsymbol{\Phi}_\mathrm{bb} \end{bmatrix}}_{\boldsymbol{\Phi}} \begin{bmatrix} \boldsymbol{i}_\mathrm{g}(k) \\ \mathbf{x}_\mathrm{r}(k) \end{bmatrix} + \underbrace{\begin{bmatrix} 0 \\ \boldsymbol{\Gamma}_\mathrm{r} \end{bmatrix}}_{\boldsymbol{\Gamma}_\mathrm{c}} \boldsymbol{u}_\mathrm{c,ref}(k) \tag{3.6}$$

where $\boldsymbol{\phi}_\mathrm{aa}$, $\boldsymbol{\Phi}_\mathrm{ab}$, $\boldsymbol{\Phi}_\mathrm{ba}$, and $\boldsymbol{\Phi}_\mathrm{bb}$ are the submatrices of $\boldsymbol{\Phi}$ and $\boldsymbol{\Gamma}_\mathrm{r}$ is the submatrix of $\boldsymbol{\Gamma}_\mathrm{c}$, cf. (3.2). The grid voltage $\boldsymbol{e}_\mathrm{g}$ is considered as an unknown disturbance. Following the standard approach (Franklin et al., 1997), the reduced-order observer can be written as

$$\hat{\mathbf{x}}_\mathrm{r}(k) = \boldsymbol{\Phi}_\mathrm{bb}\hat{\mathbf{x}}_\mathrm{r}(k-1) + \boldsymbol{\Phi}_\mathrm{ba}\boldsymbol{i}_\mathrm{g}(k-1) + \boldsymbol{\Gamma}_\mathrm{r}\boldsymbol{u}_\mathrm{c,ref}(k-1) + \mathbf{K}_\mathrm{o}\boldsymbol{e}_\mathrm{o}(k) \tag{3.7}$$

$$\boldsymbol{e}_\mathrm{o}(k) = \boldsymbol{i}_\mathrm{g}(k) - \boldsymbol{\phi}_\mathrm{aa}\boldsymbol{i}_\mathrm{g}(k-1) - \boldsymbol{\Phi}_\mathrm{ab}\hat{\mathbf{x}}_\mathrm{r}(k-1) \tag{3.8}$$

where $\mathbf{K}_\mathrm{o}$ is the observer gain and $\boldsymbol{e}_\mathrm{o}$ is the estimation error of the current. Since the grid voltage is considered as an unknown disturbance, the estimation error is nonzero in the steady state. However, the internal dynamics of the estimated states are correctly presented.

3.1.3 Integrator-Based Design

Figure 3.2 shows the integrator-based current control structure. The control law is

$$\begin{aligned} \boldsymbol{x}_\mathrm{i}(k+1) &= \boldsymbol{x}_\mathrm{i}(k) + \boldsymbol{i}_\mathrm{g,ref}(k) - \boldsymbol{i}_\mathrm{g}(k) \\ \boldsymbol{u}_\mathrm{c,ref}(k) &= \boldsymbol{k}_\mathrm{t}\boldsymbol{i}_\mathrm{g,ref}(k) - \mathbf{K}_\mathrm{fi}\hat{\mathbf{x}}(k) + \boldsymbol{k}_\mathrm{i}\boldsymbol{x}_\mathrm{i}(k) \end{aligned} \tag{3.9}$$

where $\boldsymbol{k}_\mathrm{t}$ is the feedforward gain, $\mathbf{K}_\mathrm{fi}$ is the state-feedback gain, $\boldsymbol{k}_\mathrm{i}$ is the integral gain, $\boldsymbol{x}_\mathrm{i}$ is the integral state, and $\hat{\mathbf{x}} = [\boldsymbol{i}_\mathrm{g}, \hat{\mathbf{x}}_\mathrm{r}^\mathrm{T}]^\mathrm{T}$ is the state vector consisting of the measured state $\boldsymbol{i}_\mathrm{g}$ and estimated states $\hat{\mathbf{x}}_\mathrm{r} = [\hat{\boldsymbol{u}}_\mathrm{f}, \hat{\boldsymbol{i}}_\mathrm{c}, \hat{\boldsymbol{u}}_\mathrm{c}]^\mathrm{T}$. The integral state $\boldsymbol{x}_\mathrm{i}$ in the control law (3.9) eliminates the steady-state control error. The reference feedforward produces an additional zero in the numerator polynomial of the reference-tracking transfer function, as described in detail in Publication III.

The control structure shown in Figure 3.2 is based on the grid current measurement only. The unknown states $\hat{\mathbf{x}}_\mathrm{r} = [\hat{\boldsymbol{u}}_\mathrm{f}, \hat{\boldsymbol{i}}_\mathrm{c}, \hat{\boldsymbol{u}}_\mathrm{c}]^\mathrm{T}$ are estimated using

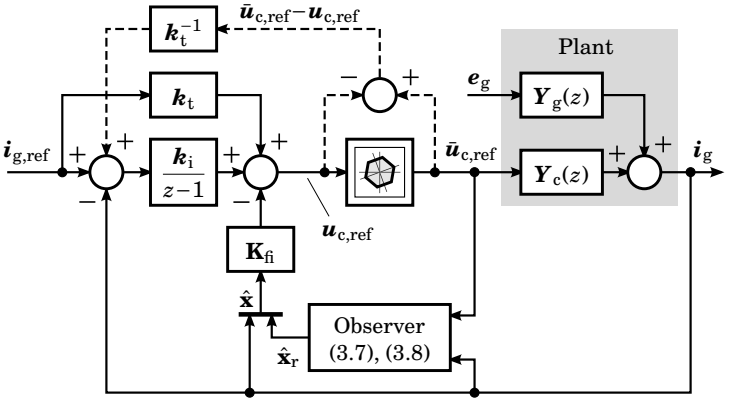

Figure 3.2. State-space current control with an integrator. The realizable voltage reference $\bar{\boldsymbol{u}}_{\mathrm{c,ref}}$ can be calculated in the current controller or in the PWM. In the linear modulation region, $\bar{\boldsymbol{u}}_{\mathrm{c,ref}} = \boldsymbol{u}_{\mathrm{c,ref}}$ holds. An anti-windup scheme is marked with dashed lines.

an observer. Here, as an example, the reduced-order observer presented in Section 3.1.2 is used. The design of the observer is also presented in Publication III. The whole control system is comparatively simple. First, the state estimate is updated using the observer [cf. (3.7) and (3.8)]. Then, the converter voltage reference is computed using the control law (3.9). It is worth mentioning that the integrator-based control structure can be extended to double-frequency current control, as shown later in Section 3.2 as well as in Publication III.

3.1.4 Disturbance-Observer-Based Design

Figure 3.3 shows the disturbance-observer-based current control structure. The control scheme uses an estimated disturbance $\hat{\boldsymbol{w}}$ in the control law. Since the grid voltage is considered as an unknown disturbance, an input-equivalent disturbance is used in this model, as explained by Pérez-Estévez et al. (2017) as well as in Publication III. In accordance with Figure 3.3, the control law is

$$\boldsymbol{u}_{\mathrm{c,ref}}(k) = \boldsymbol{k}_{\mathrm{f}}\boldsymbol{i}_{\mathrm{g,ref}}(k) - \mathbf{K}_{\mathrm{fd}}\hat{\mathbf{x}}(k) - \hat{\boldsymbol{w}}(k) \tag{3.10}$$

where $\boldsymbol{k}_{\mathrm{f}}$ is the feedforward gain, $\mathbf{K}_{\mathrm{fd}}$ is the state-feedback gain, and $\hat{\mathbf{x}} = [\boldsymbol{i}_{\mathrm{g}}, \hat{\mathbf{x}}_{\mathrm{r}}^{\mathrm{T}}]^{\mathrm{T}}$ is the state vector, which contains both the measured state $\boldsymbol{i}_{\mathrm{g}}$ and estimated states $\hat{\mathbf{x}}_{\mathrm{r}} = [\hat{\boldsymbol{u}}_{\mathrm{f}}, \hat{\boldsymbol{i}}_{\mathrm{c}}, \hat{\boldsymbol{u}}_{\mathrm{c}}]^{\mathrm{T}}$.

The observer in disturbance-observer-based control is also formulated based on the system model (3.6) and augmented with the disturbance state estimate, as

$$\hat{\mathbf{x}}_{\mathrm{r}}(k) = \boldsymbol{\Phi}_{\mathrm{bb}}\hat{\mathbf{x}}_{\mathrm{r}}(k-1) + \boldsymbol{\Phi}_{\mathrm{ba}}\boldsymbol{i}_{\mathrm{g}}(k-1) + \boldsymbol{\Gamma}_{\mathrm{r}}[\boldsymbol{u}_{\mathrm{c,ref}}(k-1) + \hat{\boldsymbol{w}}(k-1)] + \mathbf{K}_{\mathrm{od}}\boldsymbol{e}_{\mathrm{o}}(k) \tag{3.11}$$

$$\hat{\boldsymbol{w}}(k) = \hat{\boldsymbol{w}}(k-1) + \boldsymbol{k}_{\mathrm{w}}\boldsymbol{e}_{\mathrm{o}}(k) \tag{3.12}$$

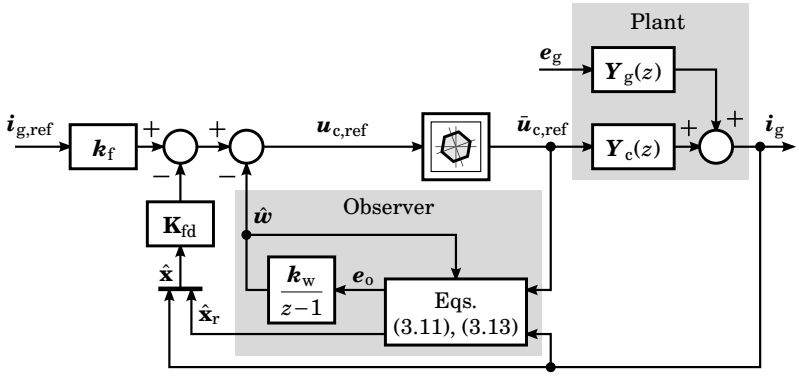

Figure 3.3. State-space current control with a disturbance observer.

$$\boldsymbol{e}_o(k) = \boldsymbol{i}_g(k) - \boldsymbol{\phi}_{aa}\boldsymbol{i}_g(k-1) - \boldsymbol{\Phi}_{ab}\hat{\mathbf{x}}_r(k-1) \tag{3.13}$$

where $\mathbf{K}_{od}$ and $\boldsymbol{k}_w$ are the observer gains, and $\boldsymbol{e}_o$ is the estimation error of the grid current. The disturbance state estimate $\hat{\boldsymbol{w}}$ is obtained by integrating the estimation error $\boldsymbol{e}_o$. Due to the integral action, the estimation error becomes zero in the steady state.

The observer is of the fourth order in the disturbance-observer-based control, whereas it is of the third order in the integrator-based control. However, including the observer and the control law, the order of the whole controller is the same in both control structures.

3.1.5 Equivalence of the Controllers

The integrator-based controller is found to be mathematically equivalent to the disturbance-observer-based controller, as shown in Publication III. A common framework, based on a 2DOF control structure (Skogestad and Postlethwaite, 1996), is developed for both current controllers and the conditions for equivalence are derived. The common framework is shown in Figure 3.4, which consists of a feedback controller $\boldsymbol{C}(z)$, a reference prefilter $\boldsymbol{F}(z)$, and the open-loop transfer functions $\boldsymbol{Y}_c(z)$ and $\boldsymbol{Y}_g(z)$, cf. (3.4) and (3.5). According to Figure 3.4, the closed-loop response is

$$\boldsymbol{i}_g(z) = \underbrace{\frac{\boldsymbol{F}(z)\boldsymbol{C}(z)\boldsymbol{Y}_c(z)}{1+\boldsymbol{C}(z)\boldsymbol{Y}_c(z)}}_{\boldsymbol{G}(z)}\boldsymbol{i}_{g,ref}(z) + \underbrace{\frac{\boldsymbol{Y}_g(z)}{1+\boldsymbol{C}(z)\boldsymbol{Y}_c(z)}}_{\boldsymbol{Y}(z)}\boldsymbol{e}_g(z) \tag{3.14}$$

where $\boldsymbol{G}(z)$ is the reference-tracking transfer function and $\boldsymbol{Y}(z)$ is the disturbance-rejection admittance.

The closed-loop systems obtained from two state-space control structures, presented in Sections 3.1.3 and 3.1.4, become identical for the same plant if the following two conditions are met: 1) feedback controllers in both designs are equal; and 2) reference prefilters in both designs are equal. These conditions are further expressed in Publication III in terms of characteristic polynomials of the systems. It has been shown that the integrator-based

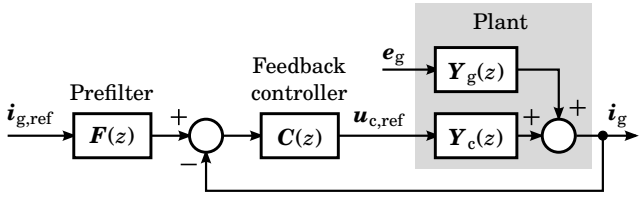

Figure 3.4. 2DOF current control structure. The converter voltage reference is assumed to stay in the linear modulation region, i.e., $\bar{\boldsymbol{u}}_{c,ref} = \boldsymbol{u}_{c,ref}$.

and disturbance-observer-based controllers become identical if the feedforward gains are selected to be equal, the feedforward zero is placed to cancel the pole originating from the integral action, and the closed-loop poles are identically placed. Though the reduced-order observer is used as an example, similar equivalence conditions also hold for full-order observers.

3.1.6 Control Tuning

A flowchart of current control tuning by means of an analytical approach is provided by Kukkola et al. (2015). Figure 3.5 shows a similar flowchart for computing the controller gains numerically according to the direct pole-placement method, which is used in Publications I-IV. At the design stage, the nominal parameters of the LCL filter are typically known. However, the grid inductance L_g is often unknown and time-varying. In the literature, the controller gains are mostly calculated assuming a strong grid ($L_g = 0$) under nominal conditions (Kukkola et al., 2015; Pérez-Estévez et al., 2017). Nevertheless, any other values of L_g can be used. For example, a very weak grid assumption ($L_g = 1$ p.u.) is used in the control tuning in Publication II. It is to be noted that a large grid inductance assumption leads to large control gains for a given control bandwidth.

The sampling frequency f_s also affects the stability of current control. Two distinct stability regions of the LCL filter resonance, below and above the critical resonance frequency (i.e., $f_s/6$), are identified by Parker et al. (2014). In Publication II, the robustness of the current controller is examined at two different sampling frequencies for which the critical resonance frequency becomes lower and higher than the filter resonance frequency. A stable system can be achieved irrespective of the ratio of the filter resonance frequency to the sampling frequency, which is not possible with PI or PR controllers. After selecting L_g and f_s, the matrices $\boldsymbol{\Phi}$ and $\boldsymbol{\Gamma}_c$ are computed. These matrices are used in the observer and in control gain calculation.

When selecting control and observer pole locations, compromises between obtained control gains, robustness, and dynamic performance must be made. Using the direct pole-placement method presented in Publications I-IV, the poles of the closed-loop system are placed at the desired locations

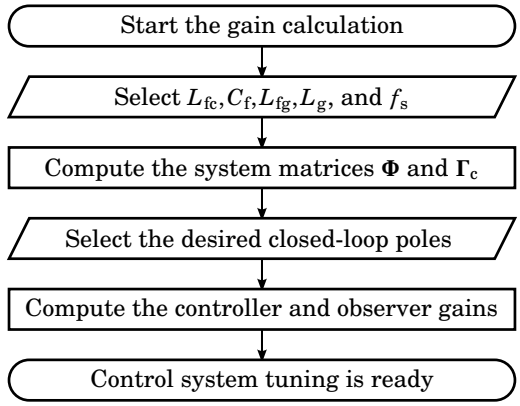

Figure 3.5. Flowchart of control tuning.

with reasonable control gains. The pole-placement strategy is based on the radial projection for the resonance damping of the LCL filter. The design guidelines, presented in Publications I-IV, provide good dynamic performance and robustness against grid strength variations.

3.2 Double-Frequency Current Control

The controllers presented in Sections 3.1.3 and 3.1.4 are unsuitable for unbalanced grid conditions, since they control only the positive sequence of the grid current with zero steady-state error. Under unbalanced grid conditions, both positive and negative sequences of the grid current should be simultaneously controlled. In the literature, a conventional method for double-frequency control is the dual current controller (Hong-Seok Song and Kwanghee Nam, 1999; Yongsug Suh and Lipo, 2006; Ahmed et al., 2011; Reyes et al., 2012). This structure is also known as double synchronous reference frame (DSRF) control (Yepes et al., 2014). In the DSRF controller, the positive sequence is controlled in the positive synchronous reference frame, while the negative sequence is controlled in the negative synchronous reference frame. The DSRF control method requires a total of four separate PI controllers with cross dq-axis decoupling technique. Hence, the control system becomes complicated. Moreover, the tuning of the control system is not straightforward. A trade-off between the dynamic performance and closed-loop stability needs to be considered in the control tuning (Hong-Seok Song and Kwanghee Nam, 1999). On the other hand, the state-space control with direct pole-placement method is comparatively simple (Pérez-Estévez et al., 2017). Both of the state-space control structures, the integrator- and disturbance-observer-based, can be extended to the double-frequency current control, which are presented in the following sections.

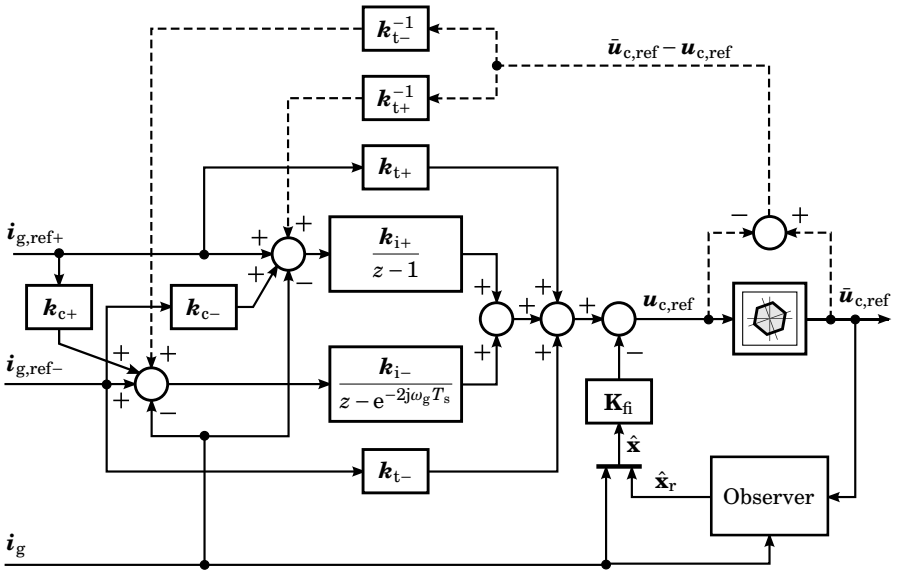

Figure 3.6. Integrator-based design of a double-frequency current controller. The anti-windup mechanism for both positive and negative sequences is marked with dashed lines.

3.2.1 Integrator-Based Control

Figure 3.6 shows an integrator-based design of a double-frequency current controller. The reference current includes both the positive-sequence reference $\boldsymbol{i}_{g,ref+}$ and the negative-sequence reference $\boldsymbol{i}_{g,ref-}$. The controller needs two integrators to track the positive- and negative-sequence current references with zero steady-state control error, as proposed in Publication III. The control design is based on the concept of the reduced-order generalized integrators (ROGIs) presented by Busada et al. (2012). In accordance with Figure 3.6, the control law for the double-frequency controller is

$$\begin{aligned}
\boldsymbol{x}_{i+}(k+1) &= \boldsymbol{x}_{i+}(k) + \boldsymbol{i}_{g,ref+}(k) - \boldsymbol{i}_g(k) + \boldsymbol{k}_{c-}\boldsymbol{i}_{g,ref-}(k) \\
\boldsymbol{x}_{i-}(k+1) &= e^{-2j\omega_g T_s}\boldsymbol{x}_{i-}(k) + \boldsymbol{i}_{g,ref-}(k) - \boldsymbol{i}_g(k) + \boldsymbol{k}_{c+}\boldsymbol{i}_{g,ref+}(k) \\
\boldsymbol{u}_{c,ref}(k) &= \boldsymbol{k}_{t+}\boldsymbol{i}_{g,ref+}(k) + \boldsymbol{k}_{t-}\boldsymbol{i}_{g,ref-}(k) + \boldsymbol{k}_{i+}\boldsymbol{x}_{i+}(k) + \boldsymbol{k}_{i-}\boldsymbol{x}_{i-}(k) - \mathbf{K}_{fi}\hat{\mathbf{x}}(k)
\end{aligned} \tag{3.15}$$

where $\boldsymbol{x}_{i+}$ and $\boldsymbol{x}_{i-}$ are the integral states, $\boldsymbol{k}_{t+}$ and $\boldsymbol{k}_{t-}$ are the feedforward gains, and $\boldsymbol{k}_{i+}$ and $\boldsymbol{k}_{i-}$ are the integral gains for the positive and negative sequences, respectively. The gains $\boldsymbol{k}_{c+}$ and $\boldsymbol{k}_{c-}$ are needed to eliminate the coupling between the positive- and negative-sequence reference chains. The analytical expressions for the feedforward gains ($\boldsymbol{k}_{t+}$ and $\boldsymbol{k}_{t-}$) and decoupling gains ($\boldsymbol{k}_{c+}$ and $\boldsymbol{k}_{c-}$) are derived as a function of the integral gains and feedforward zeros in Publication III. In this structure, the same observer [(3.7) and (3.8)] is used and the rest of the design of the control method is similar to the design presented in Section 3.1.3.

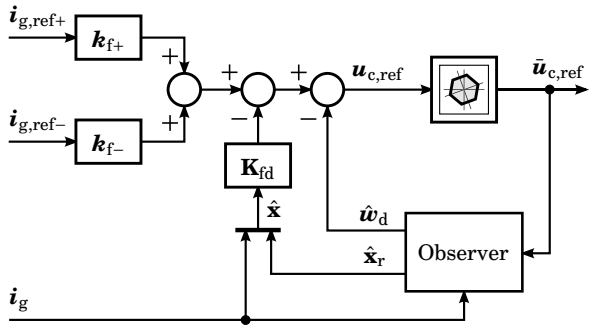

Figure 3.7. Disturbance-observer-based design of a double-frequency current controller.

3.2.2 Disturbance-Observer-Based Control

Figure 3.7 shows a disturbance-observer-based design of a double-frequency current controller. In the disturbance-observer-based control, both positive and negative sequences of the grid voltage are considered to be disturbances for the current controller, as presented by Pérez-Estévez et al. (2017). The hold-equivalent disturbance model can be expressed as

$$\mathbf{r}(k+1) = \begin{bmatrix} 1 & 0 \\ 0 & \mathrm{e}^{-2\mathrm{j}\omega_g T_s} \end{bmatrix} \mathbf{r}(k)$$

$$\boldsymbol{w}_d(k) = \begin{bmatrix} 1 & 1 \end{bmatrix} \mathbf{r}(k) \tag{3.16}$$

where $\mathbf{r} = [\boldsymbol{w}_+, \boldsymbol{w}_-]^T$ is the disturbance state vector consisting of the positive-sequence disturbance $\boldsymbol{w}_+$ and negative-sequence disturbance $\boldsymbol{w}_-$. This disturbance model is embedded into the observer analogously to (3.11)-(3.13). According to Figure 3.7, the control law can be written as

$$\boldsymbol{u}_{c,ref}(k) = \boldsymbol{k}_{f+}\boldsymbol{i}_{g,ref+}(k) + \boldsymbol{k}_{f-}\boldsymbol{i}_{g,ref-}(k) - \mathbf{K}_{fd}\hat{\mathbf{x}}(k) - \hat{\boldsymbol{w}}_d(k) \tag{3.17}$$

where $\boldsymbol{k}_{f+}$ and $\boldsymbol{k}_{f-}$ are the feedforward gains for the positive and negative sequences, respectively. The control design is similar to that explained in Section 3.1.4.

Unlike the integrator-based control, no additional decoupling gains ($\boldsymbol{k}_{c+}$ and $\boldsymbol{k}_{c-}$) are needed in the disturbance-observer-based control. The integrator-based control structure becomes more complex as compared to the disturbance-observer-based control, due to the required anti-windup mechanisms for both positive and negative sequences (cf. Figure 3.6). No additional anti-windup scheme is needed in the disturbance-observer-based control.

Both double-frequency controllers are shown to be equivalent in a similar manner as the single-frequency controllers, as explained in Section 3.1.5. They are equal if $\boldsymbol{k}_{t+} = \boldsymbol{k}_{f+}$, $\boldsymbol{k}_{t-} = \boldsymbol{k}_{f-}$, the feedforward zeros cancel the poles originating from the integral actions, and the closed-loop poles are

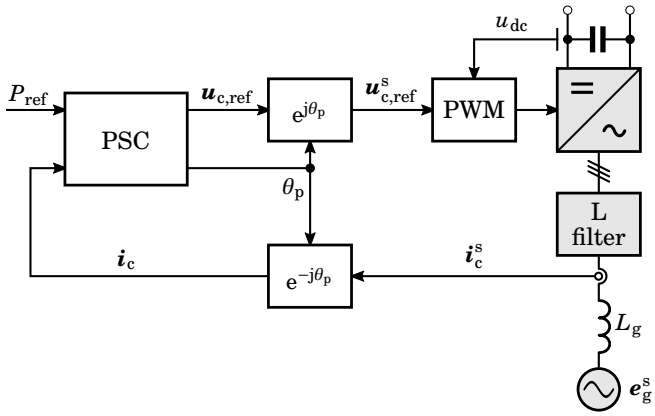

Figure 3.8. Control system of a grid converter with PSC. The converter is equipped with an L filter and connected to an inductive grid at the PCC.

identical. The equivalence for the double-frequency current controllers is shown in detail in Publication III.

3.3 Power-Synchronization Control

Figure 3.8 shows a structure of control system for grid converters with power-synchronization control (PSC). Unlike the control system shown in Figure 3.1, no PLL is required in PSC. The PSC was conceived by Zhang et al. (2010) in order to enable a stable connection of VSC connected to weak grids. The PSC belongs to grid-forming control schemes (Pan et al., 2020), in which the dynamics of a synchronous machine can be emulated (Beck and Hesse, 2007). To synchronize VSCs with the grid, an internal power-synchronization mechanism (i.e., a transient power transfer) in AC systems is utilized. The PSC has been proposed for different applications, such as high-voltage direct-current (HVDC) transmission systems (Zhang et al., 2011a,b; Khazaei et al., 2018), solar PV systems (Radwan and Mohamed, 2016), and wind energy systems (Mitra et al., 2014; Nanou and Papathanassiou, 2016). This method has also been tested for a grid-connected VSC equipped with an LCL filter (Harnefors et al., 2020). The active-power control loop of PSC can also be cascaded with outer control loops. For example, AC-voltage control, reactive-power control, and DC-link voltage control are included in the control system presented by Zhang et al. (2010).

3.3.1 PSC Design

Figure 3.9 shows the block diagram of PSC. In PSC, the active power is directly controlled by a power-synchronization loop (PSL). The PSL is

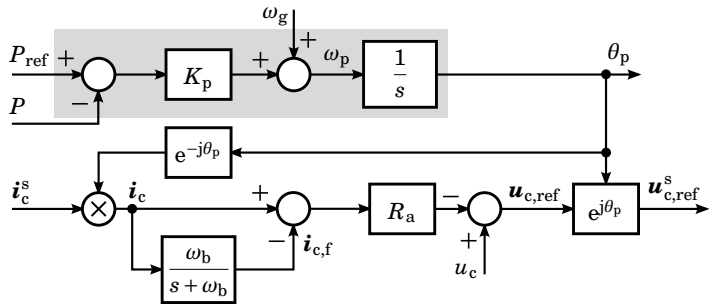

Figure 3.9. Grid synchronization and active-power control with PSC.

shown inside the gray block in Figure 3.9. The PSL maintains synchronism between the VSC and the grid. The output of the PSL provides the synchronization angle θ_p. The angle θ_p is governed by the active-power control law as

$$\frac{d\theta_p}{dt} = \omega_g + K_p(P_{ref} - P) \tag{3.18}$$

where K_p is the active-power control gain, P_{ref} is the active power reference and P is the active output power of the converter. The active output power is computed as $P = (3/2) \cdot \mathrm{Re}\{\boldsymbol{u}^s_{c,ref}(\boldsymbol{i}^s_c)^*\}$, where $\boldsymbol{u}^s_{c,ref}$ is the converter voltage reference. According to Figure 3.9, in the synchronous reference frame, the converter voltage reference can be expressed as

$$\boldsymbol{u}_{c,ref} = u_c - R_a\left(\boldsymbol{i}_c - \boldsymbol{i}_{c,f}\right) \tag{3.19}$$

where u_c is the converter voltage magnitude (normally 1 p.u.), $\boldsymbol{i}_{c,f}$ is the low-pass filtered converter current, and R_a is the active resistance. The active resistance is included in the control system in order to damp the oscillations in current as well as in power. The current $\boldsymbol{i}_{c,f}$ can be expressed as

$$\boldsymbol{i}_{c,f} = \frac{\omega_b}{s+\omega_b}\boldsymbol{i}_c \tag{3.20}$$

where ω_b is the bandwidth of the low-pass filter. For the PWM, the converter voltage reference $\boldsymbol{u}_{c,ref}$ is transformed to the stationary reference frame using the synchronization angle θ_p given by (3.18).

The PSC inherently adds a frequency droop to the active power reference (Liu et al., 2016). When the instantaneous angular frequency $\omega_p = d\theta_p/dt$ deviates from the fundamental angular grid frequency ω_g, the active power in the steady state becomes

$$P = P_{ref} + \frac{1}{K_p}\left(\omega_g - \omega_p\right). \tag{3.21}$$

In Publication V, a robust design recommendation for the active-power control gain K_p is presented, by which adequate stability margins are always obtained irrespective of the SCR and of the operating conditions. Selection recommendations for ω_b and R_a are also provided. Furthermore,

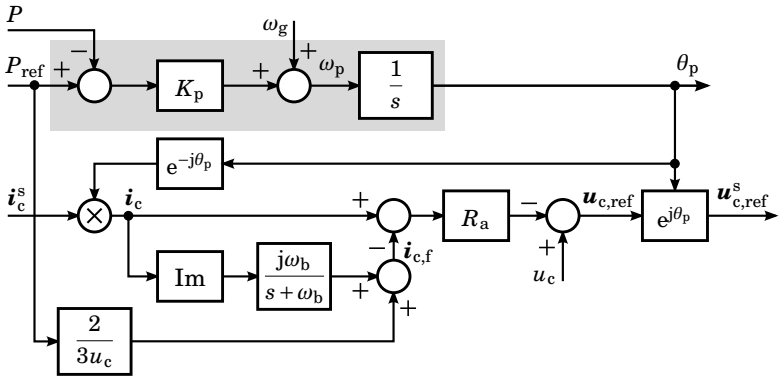

Figure 3.10. Grid synchronization and active-power control with reference-feedforward PSC. The PSL is shown inside the gray block.

the proposed design is compared to design based on the principle virtual synchronous machine. As also demonstrated in Publication V, the proposed design recommendation for the active-power control gain is suitable for cascaded DC-link voltage control. It is to be noted that, due to the limited bandwidth of the closed-loop system, the PSC has been found to be inferior to VCC for strong grids.

In the control system, an embedded current limitation scheme is included in order to prevent over-current flowing through the VSC. The current limitation scheme is transparent during normal operation. For digital implementation of the control, the PSC is discretized using the forward-difference method.

3.3.2 Reference-Feedforward PSC

In Publication VI, an enhancement of the PSC is proposed, called reference-feedforward PSC. Figure 3.10 shows the block diagram of the reference-feedforward PSC. In this scheme, a modification of the PSC is realized by adding a feedforward of scaled P_{ref} to set the d component of $\boldsymbol{i}_{\mathrm{c,f}}$. The q component of $\boldsymbol{i}_{\mathrm{c,f}}$ is obtained via a low-pass filtering of the q component of $\boldsymbol{i}_{\mathrm{c}}$. The current $\boldsymbol{i}_{\mathrm{c,f}}$ can be expressed as

$$\boldsymbol{i}_{\mathrm{c,f}} = \frac{2}{3}\frac{P_{\mathrm{ref}}}{u_{\mathrm{c}}} + \mathrm{j}\frac{\omega_{\mathrm{b}}}{s+\omega_{\mathrm{b}}}\mathrm{Im}\{\boldsymbol{i}_{\mathrm{c}}\}. \tag{3.22}$$

The synchronization is maintained using (3.18) and the converter voltage reference is computed using (3.19).

The same design recommendations for the PSC, presented in Publication V, are used for the reference-feedforward PSC in Publication VI. The robust stability irrespective of the grid strength is achieved. With the reference-feedforward PSC, the step-response ringing and overshoot observed in the PSC are eliminated. In addition, the proposed design increases the closed-loop bandwidth under strong grid conditions, which allows a shorter

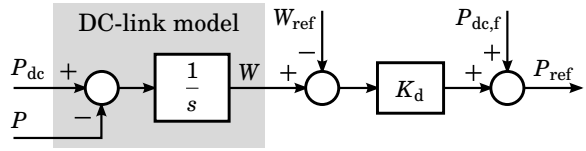

Figure 3.11. DC-link voltage control.

step-response rise time, resulting in a similar performance to that of VCC.

3.4 DC-Link Voltage Control

Figure 3.11 shows the block diagram of a DC-link voltage control. DC-link voltage control can be added as an outer loop in cascade with a current control loop in VCC (Hur et al., 2001; Harnefors et al., 2007) as well as with an active-power control loop in PSC (Zhang et al., 2010). The DC-link voltage is controlled using the energy stored in the DC-link capacitor W as an auxiliary state variable. According to Figure 3.11, the DC-link voltage control law can be defined as

$$P_{\mathrm{ref}} = K_{\mathrm{d}}(W - W_{\mathrm{ref}}) + P_{\mathrm{dc,f}} \tag{3.23}$$

where K_{d} is the DC-link voltage control gain, $W_{\mathrm{ref}} = (1/2)C_{\mathrm{dc}}u_{\mathrm{dc,ref}}^2$ is the desired energy stored in the DC-link capacitor, and $P_{\mathrm{dc,f}}$ is the low-pass filtered DC-source power P_{dc} used as a feed-forward. The DC-source power P_{dc} is often known and thus can easily be fed forward. A similar approach is also used by Harnefors et al. (2007), but with a PI controller instead of the proportional control used in (3.23). Alternatively, a conventional PI controller without the feed-forward DC-source power $P_{\mathrm{dc,f}}$ can also be used, as demonstrated by Hur et al. (2001); Zhang et al. (2010); Harnefors et al. (2016).

DC-link voltage control provides the active power reference P_{ref} for the current reference calculation or the d component of the current reference for the current controller in VCC. The power reference P_{ref}, generated from DC-link voltage control, can be used in the active-power control loop in the PSC (cf. Figure 3.9) and reference-feedforward PSC (cf. Figure 3.10). In publication V, an analytical design recommendation for the DC-link voltage control gain is given for the PSC, in which the robustness of the closed-loop system is guaranteed. With this design recommendation, sufficiently large stability margins are achieved irrespective of the SCR. The same design recommendation is also applicable for the reference-feedforward PSC presented in Publication VI.

3.5 Control System Implementation Aspects

The following subsections include some control system implementation aspects that were not explained in detail in the publications.

3.5.1 Voltage Saturation and Anti-Windup

The converter saturates when the converter voltage reference reaches the maximum available voltage, i.e., the border of the voltage hexagon (Holtz, 1994). The converter may saturate during startup and shutdown as well as during a large change in the operating point. Therefore, the converter voltage reference should be limited. In this thesis, the converter voltage reference is limited to the maximum allowable range in the linear modulation region. In synchronous coordinates, the limited voltage reference is calculated as

$$\bar{\boldsymbol{u}}_{\mathrm{c,ref}} = \begin{cases} \boldsymbol{u}_{\mathrm{c,ref}}, & \text{if } |\boldsymbol{u}_{\mathrm{c,ref}}| \leq u_{\max} \\ \dfrac{\boldsymbol{u}_{\mathrm{c,ref}}}{|\boldsymbol{u}_{\mathrm{c,ref}}|} u_{\max}, & \text{if } |\boldsymbol{u}_{\mathrm{c,ref}}| > u_{\max} \end{cases} \tag{3.24}$$

where $u_{\max} = u_{\mathrm{dc}}/\sqrt{3}$ is the maximum voltage magnitude that can be achieved in the linear modulation region (Kazmierkowski et al., 2002). The limited voltage reference $\bar{\boldsymbol{u}}_{\mathrm{c,ref}}$ is calculated in the current controller. As can be seen from (3.24), $\bar{\boldsymbol{u}}_{\mathrm{c,ref}} = \boldsymbol{u}_{\mathrm{c,ref}}$ holds in the linear modulation region.

The integral term in the controller accumulates the control error when $|\boldsymbol{u}_{\mathrm{c,ref}}| > u_{\max}$, which is known as the integrator windup. The integrator windup leads to poor transient response, e.g., undesired overshoots in the output current (Åström and Wittenmark, 1997). To prevent the integrator windup in the current controllers presented in Sections 3.1.3 and 3.1.4, an anti-windup mechanism needs to be implemented.

An anti-windup scheme, which is based on the limited voltage reference $\bar{\boldsymbol{u}}_{\mathrm{c,ref}}$ (Peng et al., 1996), is used in the integrator-based control shown in Figure 3.2. This anti-windup scheme has no effect in the linear modulation region. Contrarily to the integrator-based control, no additional anti-windup scheme is needed in the disturbance-observer-based control. The observer estimates the disturbance state in the disturbance-observer-based control, as can be seen from Figure 3.3. The converter-voltage saturation is also taken into account, meaning that the observer (3.11) uses $\bar{\boldsymbol{u}}_{\mathrm{c,ref}}$ instead of $\boldsymbol{u}_{\mathrm{c,ref}}$. This scheme inherently provides an anti-windup mechanism and is known as anti-windup with an observer (Åström and Wittenmark, 1997; Goodwin et al., 2000).

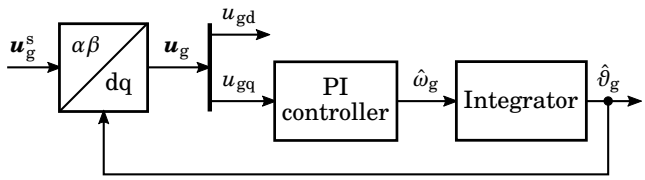

Figure 3.12. Block diagram of a PLL used in the control system shown in Figure 3.1.

3.5.2 PLL

A PLL is needed in VCC in order to synchronize the converter with the grid. Figure 3.12 shows the block diagram of a simple PI-control-based PLL operating in synchronous coordinates (Kaura and Blasko, 1997). The PLL tracks the PCC-voltage angle ϑ_g and synchronizes the converter with the grid based on this angle. In this case, the PLL drives the error signal u_{gq} to zero, leading to $\hat{\vartheta}_g = \vartheta_g$ and $u_{gd} = u_g$ in ideal conditions. Additional features and filters could be included in the PLL, for example, as presented by Han et al. (2016).

The angle ϑ_g is not directly used in the control as the angle ϑ_g can be noisy. The PLL filters noise above the PLL bandwidth. In weak grids, the PCC voltage is not stiff and it varies to a great extent with the variations in the current flowing to the grid (Zhang, 2010; Wu et al., 2017). A fast PLL cannot be used as it makes the system very sensitive to the changes in the PCC voltage. Therefore, a slow PLL with the bandwidth of $2\pi \cdot 2$ rad/s is used in Publications I-IV in order to avoid coupling between the current control dynamics and the PLL dynamics (Zhou and Gole, 2012; Zhou et al., 2014; Mortazavian and Mohamed, 2018).

The PLL is also needed in practice in PSC. In the control system in PSC, the PLL is used as a backup to provide grid synchronization during severe grid faults (Zhang et al., 2010; Wu and Wang, 2019). The backup PLL can also be used for synchronization of VSCs before they are connected to the grid. The PLL is transparent during normal operation. The same PI-control-based PLL, shown in Figure 3.12, is used in Publications V and VI.

3.5.3 Reference Calculation

The grid current is chosen as the controlled variable in the control system shown in Figure 3.1 as well as in both state-space control structures presented in Sections 3.1.3 and 3.1.4. The grid current reference $\boldsymbol{i}_{g,ref} = i_{gd,ref} + \mathrm{j} i_{gq,ref}$ can be directly set for the current controller, as applied in Publications II-IV. The current reference components $i_{gd,ref}$ and $i_{gq,ref}$ can also be set as a function of the active and reactive power references (i.e.

P_{ref} and Q_{ref}), respectively, as

$$i_{\mathrm{gd,ref}} = \frac{2}{3}\frac{P_{\mathrm{ref}}}{u_{\mathrm{g,ref}}} \quad \text{and} \quad i_{\mathrm{gq,ref}} = -\frac{2}{3}\frac{Q_{\mathrm{ref}}}{u_{\mathrm{g,ref}}} \tag{3.25}$$

where $u_{\mathrm{g,ref}}$ is the reference for the PCC voltage. The active power reference P_{ref} could be the output of the DC-link voltage controller, if such is used.

The reactive power is controlled to be zero for unity power factor operation, i.e., $i_{\mathrm{gq,ref}} = 0$. An AC-voltage controller is necessary for operation in weak grids (Arani and Mohamed, 2017; Strachan and Jovcic, 2010). The AC-voltage controller enables the converter to transfer 1 p.u. of the active power to the grid and maintains the PCC voltage at 1 p.u., as shown by Huang et al. (2015) and Egea-Alvarez et al. (2015). In accordance with Figure 3.1, the AC-voltage controller provides the reference for the reactive-power-producing current component $i_{\mathrm{gq,ref}}$. In Publication I, an integral AC-voltage controller is used for the sake of simplicity. The reactive-power-producing current component is

$$i_{\mathrm{gq,ref}}(z) = \frac{T_{\mathrm{s}} k_{\mathrm{i,ac}}}{z-1}\left[u_{\mathrm{g,ref}}(z) - u_{\mathrm{g}}(z)\right] \tag{3.26}$$

where $k_{\mathrm{i,ac}}$ is the integral gain.

The grid current can indirectly be controlled by controlling the converter current, as demonstrated in Publication II. In this case, the converter current reference $\boldsymbol{i}_{\mathrm{c,ref}}$ has to be expressed as a function of the grid current reference $\boldsymbol{i}_{\mathrm{g,ref}}$ as

$$\boldsymbol{i}_{\mathrm{c,ref}} = (1 - \omega_{\mathrm{g}}^2 C_{\mathrm{f}} L_{\mathrm{fg}})\boldsymbol{i}_{\mathrm{g,ref}} + \mathrm{j}\omega_{\mathrm{g}} C_{\mathrm{f}} u_{\mathrm{g,ref}} \tag{3.27}$$

where the PCC voltage reference is $u_{\mathrm{g,ref}} = \sqrt{E_{\mathrm{g}}^2 - (\omega_{\mathrm{g}} L_{\mathrm{g}} i_{\mathrm{gd,ref}})^2} - \omega_{\mathrm{g}} L_{\mathrm{g}} i_{\mathrm{gq,ref}}$. A similar strategy for calculating the converter current reference has also been used by Kukkola and Hinkkanen (2014).

4. Experimental Setup

This chapter describes the experimental test setup used in the publications. It also briefly explains the implementation of the control algorithms in a dSPACE system.

4.1 Setup Description

The block diagram of the experimental setup is shown in Figure 4.1. The setup was used to experimentally verify the control methods presented in Publications I-IV. The setup has two back-to-back connected 12.5-kVA converters (ABB ACSM1). The converter under test can be directly connected to the 400-V, 50-Hz grid or to the 50-kVA four-quadrant three-phase programmable grid simulator (Regatron TopCon TC.ACS) via external inductors (if such is used). The Regatron grid simulator can be used to produce various grid-fault conditions and harmonics. The load converter system, consisting of a converter (ABB ACSM1) and an LCL filter, is used

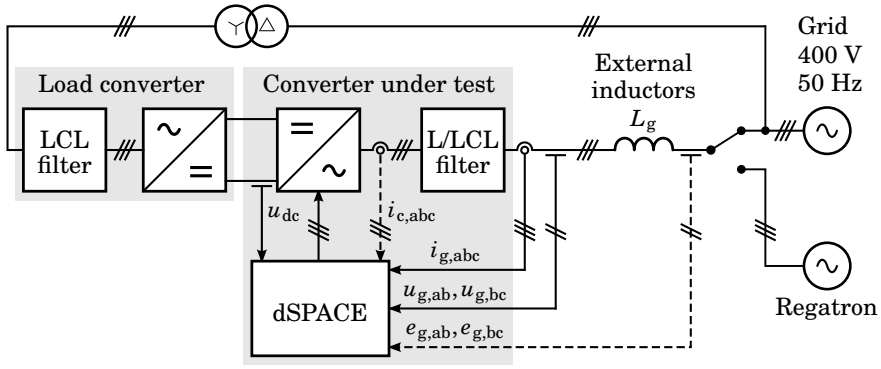

Figure 4.1. Block diagram of the experimental setup. The Regatron grid simulator can be used to emulate grid voltage disturbances, e.g., grid-voltage dips and harmonics. The external inductors L_g is used in order to emulate weak grids. The converter currents $i_{c,abc}$ and the grid voltages $e_{g,ab}$,$e_{g,bc}$ (marked with dashed lines) can be measured.

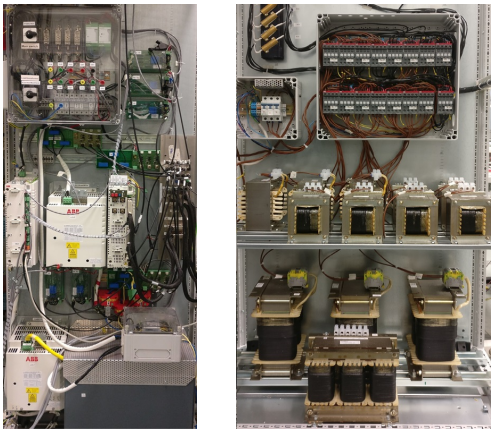

(a) (b)

Figure 4.2. Photographs: (a) experimental setup; and (b) external inductors used to emulate different grid conditions.

Table 4.1. Nominal parameters of a 12.5-kVA converter system

Parameter	Value	Value (p.u.)
L filter		
Inductance L_{f}	4.0 mH	0.1
LCL filter		
Converter-side inductance L_{fc}	3.3 mH	0.081
Grid-side inductance L_{fg}	3.0 mH	0.074
Capacitance C_{f}	8.8 μF	0.036
Grid		
Base inductance	40.2 mH	1
Angular frequency ω_{g}	$2\pi\cdot$ 50 rad/s	1
Voltage E_{g} (phase-neutral, peak)	$\sqrt{2/3}\cdot$ 400 V	1
Converter		
Rated current (peak)	$\sqrt{2}\cdot$ 18.3 A	1
DC-link voltage u_{dc}	650 V	2
DC-link capacitance C_{dc}	2.1 mF	8.3

as a voltage or power source. An isolation transformer is used to connect the load converter system to the grid. The photograph of the experimental setup is shown in Figure 4.2(a). The external inductors, used to emulate different grid conditions, are shown in Figure 4.2(b). The nominal parameters of the grid and the converter system are given in Table 4.1.

4.2 Implementation

The control algorithms were first programmed in a Matlab/Simulink environment and then implemented in a dSPACE DS1006 processor board. In

order to generate the switching signals for the converter under test, a PWM interface of the dSPACE system was used. The sampling period T_s and the duty ratios $\boldsymbol{d}_\mathrm{abc}$ are the inputs to the PWM interface. The currents and the voltages are measured using external closed-loop Hall-effect transducers (LEM). The sampling of the measured quantities was synchronized with the PWM.

The original control board of the converter under test is replaced with an interface board for use with a dSPACE system. The interface board passes the switching signals to the converter and provides necessary protection, for example, against the over-current and over-voltage. In addition, a dead-time of 2 μs is generated in the interface board before passing the switching signals to the converter.

The converter under test is equipped either with an L filter or an LCL filter. The LCL filter is used in the experiments in Publications I-IV whereas the L filter is used in Publications V and VI. The nominal parameters of the filters are given in Table 4.1.

5. Summaries of Publications

This chapter presents the abstracts of the publications and the scientific contributions of this thesis.

5.1 Abstracts

The abstracts of the publications are given in this section.

Publication I

This paper deals with state-feedback current control for power converters, which are equipped with an LCL filter and connected to a weak grid. The grid-side current is measured and other states needed by the current controller are estimated using a reduced-order observer. The control system is designed directly in the discrete-time domain. The gains of the control system are calculated using direct pole placement, assuming a strong grid. Recommendations for the nominal pole locations are given. The results show that the control system is robust against the unknown grid impedance, ranging from strong to very-weak grid conditions. The proposed design is validated by means of experiments.

Publication II

This paper deals with discrete-time state-space current control of three-phase converters equipped with an LCL filter. Either the converter or grid current is measured and the unknown states are estimated using a reduced-order observer. The stability and dynamic performance of the control designs based on these two current measurement options are compared by means of analysis and experiments at different sampling frequencies and under varying grid conditions, ranging from strong to very weak. Equal reference-tracking performance under nominal conditions is used as a basis for comparison between these two options. If a strong

grid is assumed in the control tuning, the controller based on the grid current measurement (GCM) is found to be more robust against varying grid conditions in a wide range of sampling frequencies than the controller based on the converter current measurement (CCM). The CCM leads to better dynamic performance as compared to the GCM if the resonance frequency of the system falls below the critical resonance frequency.

Publication III

This paper deals with discrete-time state-space current controllers for three-phase grid converters equipped with an LCL filter. The integral action in the controller can be implemented either using an integrator or a disturbance observer. The results show that the disturbance-observer-based and integrator-based controllers become mathematically equal if the feedforward gains are selected to be equal, the feedforward zero is placed to cancel the pole originating from the integral action, and the closed-loop poles are placed identically. The equivalent performance in both designs is verified by means of analyses and experiments. The equivalence is also shown for double-frequency current controllers.

Publication IV

This paper studies the current-type observer, the prediction-type observer, and the reduced-order observer for discrete-time state-space current control of grid converters with an LCL filter. The robustness against parameter errors and the dynamic performance obtained with these three observers are compared by means of analysis and experiments. A unified control algorithm framework is developed to compare the structures of these observers. It is found that the reduced-order observer is merely a special case of the current-type observer. With the presented design examples, where the resonant poles are damped by means of radial projection, the use of either the current-type or the reduced-order observer leads to better disturbance rejection against the grid-voltage dip and harmonics as compared to the prediction-type observer. All the observers provide equal reference-tracking performance under nominal conditions. For a large parameter error in the grid-side inductance, the prediction-type observer leads to unstable operation of converter.

Publication V

This paper addresses robust design of the active-power and dc-link control loops of power-synchronization control. Robustness is obtained by analytic gain selections, which give large enough stability margins. The proposed design allows robust stability irrespective of the grid strength and of the

operating point, the latter with one exception. The proposed design is compared to design based on the principle virtual synchronous machine. Experiments show that the time-domain results correlate well with the frequency-domain results.

Publication VI

In this letter, an enhancement of power-synchronization control is proposed, whereby pole–zero cancellation in the closed-loop system is achieved. An effect thereof is that step-response ringing and overshoot are eliminated. For strong grids, the closed-loop bandwidth increases, allowing a shorter step-response rise time.

5.2 Scientific Contributions

The main scientific contributions of this doctoral thesis are summarized as follows:

- A robust design of a discrete-time state-space current control for grid converters is presented in Publication I. The proposed design provides stable operation from strong grid conditions to very weak grid conditions without changing the tuning of the control system.
- The stability and dynamic performance of the control designs based on two current measurement options, converter current measurement and grid current measurement, are compared at different sampling frequencies in Publication II. The effect of the grid inductance estimate on the stability of current control is presented for both current measurement options under varying grid conditions, ranging from strong to very weak.
- The mathematical equivalence of the integrator-based and disturbance-observer-based state-space current controllers is shown in Publication III in the context of grid converters. The conditions for equivalence are derived for the single- and double-frequency current controllers.
- The robustness against parameter errors and the dynamic performance obtained with the current-type observer, the prediction-type observer, and the reduced-order observer, are compared for state-space current control in Publication IV. A unified control algorithm framework is developed to show the links between apparently different observers.
- A robust design of the active-power and DC-link control loops of PSC is proposed in Publication V. Analytic selection recommenda-

tions for the active-power and DC-link control gains are presented, whereby adequate stability margins are always obtained irrespective of the grid strength and operation point. An enhancement of PSC, called reference-feedforward PSC, is proposed in Publication VI, by which the step-response ringing and overshoot observed in PSC are eliminated.

6. Conclusions

The control of VSCs plays a key role in modern power-electronic-based AC systems. This thesis presented weak-grid tolerant control methods for VSCs. Two different control methods were discussed, state-space current control and power-synchronization control (PSC). A good dynamic performance and robust operation against grid strength variations, ranging from strong to very weak, can be achieved with the proposed control designs.

A state-space current controller was directly designed in the discrete-time domain in Publications I-IV. The closed-form expressions of the discrete-time plant model, consisting of an LCL filter and an inductive grid, were used in the design and analysis of current controller and state observer. The discrete-time delays were properly included in the design. The state observer together with the state feedback enables state-space current control a flexible and convenient way to determine the dynamic performance of the closed-loop system, i.e., the current control bandwidth and the resonance damping of the LCL filter.

The control designs were based on the direct pole-placement method with the radial projection for the resonance damping of the LCL filter. The controller gains were calculated using the model parameters and dynamic performance specifications. In Publications I-IV, a strong grid was assumed in the control tuning. Publication II also proposed a design with the assumption of a very weak grid. This design approach facilitates examining of the effect of the grid inductance estimate on the stability of state-space current control. In addition, the stability analysis of the converter and grid current measurement options was examined at different sampling frequencies. Both measurement options can stabilize the system independently of the ratio of the filter resonance frequency to the sampling frequency without adding an extra damping method. The proposed designs can eliminate the fundamental limitation of single-loop PI and PR controllers.

Two state-space current control structures were presented in Publication III. A state-feedback control with integral action in the control law was used in one case, whereas in another case, the integral action was a part of the state observer. The links between these two apparently different

structures are revealed. The integrator-based controller is comparable to the disturbance-observer-based controller. Unlike in the integrator-based control, no additional anti-windup scheme is required in the disturbance-observer-based control. A benefit of using the integrator-based control is that any value of the feedforward gain leads to a zero steady-state control error. Both state-space control structures can be extended to a double-frequency current control. The double-frequency controller controls both the positive and negative sequences of the current with zero steady-state error under unbalanced grid conditions.

Three different state observers, the current-type observer, the prediction-type observer, and the reduced-order observer, were used for state-space current control in Publication IV. The robustness against the errors in the filter parameters, robustness against the grid strength variations, and the dynamic performance obtained with these three observers were demonstrated and compared. In addition, a clear link between the gains of these apparently different observers was brought out.

The state-space control presented in Publications I-IV requires the information of the LCL filter parameters. The grid inductance can be time dependent and it was considered as an unknown parameter error. The proposed control designs are robust against grid strength variations, easy to tune, and provide a good dynamic performance.

A robust design of PSC was proposed in Publications V and VI, where the converter was considered to be equipped with an L filter and connected to an inductive grid. The PSC was designed in the continuous-time domain and then discretized for the digital implementation. A robust design for the active-power control loop was addressed in Publication V. An enhancement of PSC was proposed in Publication VI, in which a high closed-loop bandwidth is achieved under strong grid conditions. The proposed designs allow robust stability irrespective of the grid strength and of the operating point.

In the state-space control, the voltage measurement at the PCC was used in the control system, e.g., in the PLL and AC-voltage controller. The control methods could be based on voltage-sensorless synchronization, which was not addressed in this thesis. A suitable topic for future research could be to examine effect of large grid impedances on the stability of voltage-sensorless control. Another related topic could be enhancement of the double-frequency current control with direct-pole placement method, such that the controller can operate in very weak grids and provide a good dynamic performance.

References

J. L. Agorreta, M. Borrega, J. López, and L. Marroyo. Modeling and control of N-paralleled grid-connected inverters with LCL filter coupled due to grid impedance in PV plants. *IEEE Trans. Power Electron.*, 26(3):770–785, Mar. 2011.

K. H. Ahmed, A. M. Massoud, S. J. Finney, and B. W. Williams. A synchronous dq frame controller via an LCL coupled filter under unbalanced three-phase voltage supply conditions. In *Proc. Int. Conf. Power Eng., Energy Elect. Drives*, pages 1–6, May 2011.

H. Akagi, E. H. Watanabe, and M. Aredes. *Instantaneous power theory and applications to power conditioning*. John Wiley & Sons, Hoboken, NJ, USA, 2007.

K. M. Alawasa and Y. A.-R. I. Mohamed. Impedance and damping characteristics of grid-connected VSCs with power synchronization control strategy. *IEEE Trans. Power Syst.*, 30(2):952–961, Mar. 2015.

M. F. M. Arani and Y. A.-R. I. Mohamed. Analysis and performance enhancement of vector-controlled VSC in HVDC links connected to very weak grids. *IEEE Trans. Power Syst.*, 32(1):684–693, Jan. 2017.

H.-P. Beck and R. Hesse. Virtual synchronous machine. In *Proc. 9th Int. Conf. Elect. Power Quality Utilisation*, pages 1–6, Oct. 2007.

R. N. Beres, X. Wang, M. Liserre, F. Blaabjerg, and C. L. Bak. A review of passive power filters for three-phase grid-connected voltage-source converters. *IEEE J. Emerg. Sel. Topics Power Electron.*, 4(1):54–69, Mar. 2016.

R. Bimarta and K. Kim. A robust frequency-adaptive current control of a grid-connected inverter based on LMI-LQR under polytopic uncertainties. *IEEE Access*, 8:28756–28773, 2020.

C. A. Busada, S. Gomez Jorge, A. E. Leon, and J. A. Solsona. Current controller based on reduced order generalized integrators for distributed generation systems. *IEEE Trans. Ind. Electron.*, 59(7):2898–2909, Jul. 2012.

C. A. Busada, S. Gomez Jorge, and J. A. Solsona. Full-state feedback equivalent controller for active damping in LCL-filtered grid-connected inverters using a reduced number of sensors. *IEEE Trans. Ind. Electron.*, 62(10):5993–6002, Oct. 2015.

S. Buso and P. Mattavelli. *Digital Control in Power Electronics*. Morgan & Claypool Publishers, 2006.

F. Cavazzana, P. Mattavelli, M. Corradin, and I. Toigo. Grid sensitivity considerations on multiple parallel inverters systems. In *Proc. IEEE 8th Int. Power Electron. Motion Control Conf. (IPEMC-ECCE Asia)*, pages 993–999, May 2016.

J. Dannehl, C. Wessels, and F. W. Fuchs. Limitations of voltage-oriented PI current control of grid-connected PWM rectifiers with LCL filters. *IEEE Trans. Ind. Electron.*, 56(2):380–388, Feb. 2009.

J. Dannehl, F. W. Fuchs, S. Hansen, and P. B. Thøgersen. Investigation of active damping approaches for PI-based current control of grid-connected pulse width modulation converters with LCL filters. *IEEE Trans. Ind. Appl.*, 46(4):1509–1517, Jul. 2010a.

J. Dannehl, F. W. Fuchs, and P. B. Thøgersen. PI state space current control of grid-connected PWM converters with LCL filters. *IEEE Trans. Power Electron.*, 25(9):2320–2330, Sep. 2010b.

D. Dong, B. Wen, D. Boroyevich, P. Mattavelli, and Y. Xue. Analysis of phase-locked loop low-frequency stability in three-phase grid-connected power converters considering impedance interactions. *IEEE Trans. Ind. Electron.*, 62(1):310–321, Jan. 2015.

M. Durrant, H. Werner, and K. Abbott. Model of a VSC HVDC terminal attached to a weak AC system. In *Proc. IEEE Conf. Control Appl. (CCA)*, pages 178–182, Jun. 2003.

A. Egea-Alvarez, S. Fekriasl, F. Hassan, and O. Gomis-Bellmunt. Advanced vector control for voltage source converters connected to weak grids. *IEEE Trans. Power Syst.*, 30(6):3072–3081, Nov. 2015.

J. H. R. Enslin and P. J. M. Heskes. Harmonic interaction between a large number of distributed power inverters and the distribution network. *IEEE Trans. Power Electron.*, 19(6):1586–1593, Nov. 2004.

G. F. Franklin, J. D. Powell, and M. L. Workman. *Digital Control of Dynamic Systems*. Addison-Wesley, Menlo Park, CA, 3rd edition, 1997.

Q. Fu, W. Du, C. Chen, H. F. Wang, and L. L. Fan. Vector and power synchronization control for connecting a VSC-MTDC to an AC power system — a comparative study of dynamic interactions between the DC and AC network based on PSCAD simulation. In *Proc. 12th IET Int. Conf. AC DC Power Trans. (ACDC)*, pages 1–6, May 2016.

I. J. Gabe, V. F. Montagner, and H. Pinheiro. Design and implementation of a robust current controller for VSI connected to the grid through an LCL filter. *IEEE Trans. Power Electron.*, 24(6):1444–1452, Jun. 2009.

G. C. Goodwin, S. F. Graebe, and M. E. Salgado. *Control System Design*. Prentice Hall, Upper Saddle River, NJ, USA, 1st edition, 2000.

Y. Han, M. Luo, X. Zhao, J. M. Guerrero, and L. Xu. Comparative performance evaluation of orthogonal-signal-generators-based single-phase PLL algorithms—a survey. *IEEE Trans. Power Electron.*, 31(5):3932–3944, May 2016.

L. Harnefors, M. Bongiorno, and S. Lundberg. Input-admittance calculation and shaping for controlled voltage-source converters. *IEEE Trans. Ind. Electron.*, 54 (6):3323–3334, Dec. 2007.

L. Harnefors, X. Wang, A. G. Yepes, and F. Blaabjerg. Passivity-based stability assessment of grid-connected VSCs—An overview. *IEEE J. Emerg. Sel. Topics Power Electron.*, 4(1):116–125, Mar. 2016.

L. Harnefors, J. Kukkola, M. Routimo, M. Hinkkanen, and X. Wang. A universal controller for grid-connected voltage-source converters. *IEEE J. Emerg. Sel. Topics Power Electron.*, early access, 2020.

J. Holtz. Pulsewidth modulation for electronic power conversion. *Proc. IEEE*, 82 (8):1194–1214, Aug. 1994.

Hong-Seok Song and Kwanghee Nam. Dual current control scheme for PWM converter under unbalanced input voltage conditions. *IEEE Trans. Ind. Electron.*, 46(5):953–959, Oct. 1999.

Y. Huang, X. Yuan, J. Hu, and P. Zhou. Modeling of VSC connected to weak grid for stability analysis of DC-link voltage control. *IEEE J. Emerg. Sel. Topics Power Electron.*, 3(4):1193–1204, Dec. 2015.

Y. Huang, X. Yuan, J. Hu, P. Zhou, and D. Wang. DC-bus voltage control stability affected by AC-bus voltage control in VSCs connected to weak AC grids. *IEEE J. Emerg. Sel. Topics Power Electron.*, 4(2):445–458, Jun. 2016.

F. Huerta, D. Pizarro, S. Cóbreces, F. J. Rodriguez, C. Girón, and A. Rodriguez. LQG servo controller for the current control of LCL grid-connected voltage-source converters. *IEEE Trans. Ind. Electron.*, 59(11):4272–4284, Nov. 2012.

F. Huerta, J. Pérez, S. Cóbreces, and M. Rizo. Frequency-adaptive multiresonant LQG state-feedback current controller for LCL-filtered VSCs under distorted grid voltages. *IEEE Trans. Ind. Electron.*, 65(11):8433–8444, Nov. 2018.

N. Hur, J. Jung, and K. Nam. A fast dynamic DC-link power-balancing scheme for a PWM converter-inverter system. *IEEE Trans. Ind. Electron.*, 48(4):794–803, Aug. 2001.

J. G. Hwang, P. W. Lehn, and M. Winkelnkemper. A generalized class of stationary frame-current controllers for grid-connected AC–DC converters. *IEEE Trans. Power Del.*, 25(4):2742–2751, Oct. 2010.

IEEE Std. 1204-1997. IEEE guide for planning DC links terminating at AC locations having low short-circuit capacities.

IEEE Std. 519-2014. IEEE recommended practice and requirements for harmonic control in electric power systems (revision of IEEE Std. 519-1992).

K. Jalili and S. Bernet. Design of LCL filters of active-front-end two-level voltage-source converters. *IEEE Trans. Ind. Electron.*, 56(5):1674–1689, May 2009.

L. Jessen, S. Günter, F. W. Fuchs, M. Gottschalk, and H. Hinrichs. Measurement results and performance analysis of the grid impedance in different low voltage grids for a wide frequency band to support grid integration of renewables. In *Proc. IEEE Energy Convers. Congr. Expo. (ECCE)*, pages 1960–1967, Sep. 2015.

Y. Jiao and F. C. Lee. LCL filter design and inductor current ripple analysis for a three-level NPC grid interface converter. *IEEE Trans. Power Electron.*, 30(9): 4659–4668, Sep. 2015.

V. Kaura and V. Blasko. Operation of a phase locked loop system under distorted utility conditions. *IEEE Trans. Ind. Appl.*, 33(1):58–63, Jan./Feb. 1997.

M. P. Kazmierkowski, R. Krishnan, and F. Blaabjerg. *Control in Power Electronics: Selected Problems*. Academic Press, San Diego, CA, USA, 2002.

S. A. Khajehoddin, M. Karimi-Ghartemani, and M. Ebrahimi. Optimal and systematic design of current controller for grid-connected inverters. *IEEE J. Emerg. Sel. Topics Power Electron.*, 6(2):812–824, Jun. 2018.

J. Khazaei, P. Idowu, A. Asrari, AB Shafaye, and L. Piyasinghe. Review of HVDC control in weak AC grids. *Electric Power Syst. Research*, 162:194–206, May 2018.

G. G. Koch, H. Pinheiro, R. C. L. F. Oliveira, and V. F. Montagner. Experimental evaluation of robust and nonrobust $\mathscr{H}_\infty$ controllers for three-phase grid-connected converters. In *Proc. Brazilian Power Electron. Conf. (COBEP)*, pages 1–6, Nov. 2017.

G. G. Koch, L. A. Maccari, R. C. L. F. Oliveira, and V. F. Montagner. Robust $\mathscr{H}_\infty$ state feedback controllers based on linear matrix inequalities applied to grid-connected converters. *IEEE Trans. Ind. Electron.*, 66(8):6021–6031, Aug. 2019.

J. Kukkola and M. Hinkkanen. Observer-based state-space current control for a three-phase grid-connected converter equipped with an LCL filter. *IEEE Trans. Ind. Appl.*, 50(4):2700–2709, Jul./Aug. 2014.

J. Kukkola and M. Hinkkanen. State observer for grid-voltage sensorless control of a grid-connected converter equipped with an LCL filter. In *Proc. 16th European Conf. Power Electron. Appl. (EPE)*, pages 1–10, Aug. 2014.

J. Kukkola and M. Hinkkanen. State observer for grid-voltage sensorless control of a converter equipped with an LCL filter: Direct discrete-time design. *IEEE Trans. Ind. Appl.*, 52(4):3133–3145, Jul. 2016.

J. Kukkola, M. Hinkkanen, and K. Zenger. Observer-based state-space current controller for a grid converter equipped with an LCL filter: Analytical method for direct discrete-time design. *IEEE Trans. Ind. Appl.*, 51(5):4079–4090, Sep./Oct. 2015.

M. Liserre, F. Blaabjerg, and S. Hansen. Design and control of an LCL-filter-based three-phase active rectifier. *IEEE Trans. Ind. Appl.*, 41(5):1281–1291, Sep./Oct. 2005.

M. Liserre, R. Teodorescu, and F. Blaabjerg. Stability of photovoltaic and wind turbine grid-connected inverters for a large set of grid impedance values. *IEEE Trans. Power Electron.*, 21(1):263–272, Jan. 2006.

J. Liu, Y. Miura, and T. Ise. Comparison of dynamic characteristics between virtual synchronous generator and droop control in inverter-based distributed generators. *IEEE Trans. Power Electron.*, 31(5):3600–3611, May 2016.

L. A. Maccari, J. R. Massing, L. Schuch, C. Rech, H. Pinheiro, V. F. Montagner, and R. C. L. F. Oliveira. Robust $\mathscr{H}_\infty$ control for grid connected PWM inverters with LCL filters. In *Proc. 10th IEEE IAS Int. Conf. Ind. Appl.*, pages 1–6, Nov. 2012.

T. Messo, J. Jokipii, A. Mäkinen, and T. Suntio. Modeling the grid synchronization induced negative-resistor-like behavior in the output impedance of a three-phase photovoltaic inverter. In *Proc. 4th IEEE Int. Symp. Power Electron. for Dist. Gen. Syst. (PEDG)*, pages 1–7, Jul. 2013.

V. Miskovic, V. Blasko, T. M. Jahns, A. H. C. Smith, and C. Romenesko. Observer-based active damping of LCL resonance in grid-connected voltage source converters. *IEEE Trans. Ind. Appl.*, 50(6):3977–3985, Nov./Dec. 2014.

P. Mitra, L. Zhang, and L. Harnefors. Offshore wind integration to a weak grid by VSC-HVDC links using power-synchronization control: A case study. *IEEE Trans. Power Del.*, 29(1):453–461, Feb. 2014.

S. Mortazavian and Y. A.-R. I. Mohamed. Dynamic analysis and improved LVRT performance of multiple DG units equipped with grid-support functions under unbalanced faults and weak grid conditions. *IEEE Trans. Power Electron.*, 33 (10):9017–9032, Oct. 2018.

S. I. Nanou and S. A. Papathanassiou. Grid code compatibility of VSC-HVDC connected offshore wind turbines employing power synchronization control. *IEEE Trans. Power Syst.*, 31(6):5042–5050, Nov. 2016.

D. Pan, X. Ruan, C. Bao, W. Li, and X. Wang. Capacitor-current-feedback active damping with reduced computation delay for improving robustness of LCL-type grid-connected inverter. *IEEE Trans. Power Electron.*, 29(7):3414–3427, Jul. 2014.

D. Pan, X. Wang, F. Liu, and R. Shi. Transient stability of voltage-source converters with grid-forming control: A design-oriented study. *IEEE J. Emerg. Sel. Topics Power Electron.*, 8(2):1019–1033, Jun. 2020.

S. G. Parker, B. P. McGrath, and D. G. Holmes. Regions of active damping control for LCL filters. *IEEE Trans. Ind. Appl.*, 50(1):424–432, Jan. 2014.

R. Peña-Alzola, M. Liserre, F. Blaabjerg, R. Sebastián, J. Dannehl, and F. W. Fuchs. Analysis of the passive damping losses in LCL-filter-based grid converters. *IEEE Trans. Power Electron.*, 28(6):2642–2646, Jun. 2013.

Youbin Peng, D. Vrancic, and R. Hanus. Anti-windup, bumpless, and conditioned transfer techniques for PID controllers. *IEEE Control Syst. Mag.*, 16(4):48–57, Aug. 1996.

D. Pérez-Estévez, J. Doval-Gandoy, A. G. Yepes, and Ó. López. Positive- and negative-sequence current controller with direct discrete-time pole placement for grid-tied converters with LCL filter. *IEEE Trans. Power Electron.*, 32(9): 7207–7221, Sep. 2017.

D. Pérez-Estévez, J. Doval-Gandoy, A. G. Yepes, Ó. López, and F. Baneira. Generalized multifrequency current controller for grid-connected converters with LCL filter. *IEEE Trans. Ind. Appl.*, 54(5):4537–4553, Sep. 2018.

A. A. A. Radwan and Y. A.-R. I. Mohamed. Power synchronization control for grid-connected current-source inverter-based photovoltaic systems. *IEEE Trans. Energy Convers.*, 31(3):1023–1036, Sep. 2016.

M. Reyes, P. Rodriguez, S. Vazquez, A. Luna, R. Teodorescu, and J. M. Carrasco. Enhanced decoupled double synchronous reference frame current controller for unbalanced grid-voltage conditions. *IEEE Trans. Power Electron.*, 27(9): 3934–3943, Sep. 2012.

A. Rodríguez-Cabero, M. Prodanovic, and J. Roldán-Pérez. Full-state feedback control of back-to-back converters based on differential and common power concepts. *IEEE Trans. Ind. Electron.*, 66(11):9045–9055, Nov. 2019.

S. Skogestad and I. Postlethwaite. *Multivarialbe Feedback Control: Analysis and Design*. John Wiley and Sons, West Sussex, England, 1996.

Y. Song, X. Wang, and F. Blaabjerg. Impedance-based high-frequency resonance analysis of DFIG system in weak grids. *IEEE Trans. Power Electron.*, 32(5): 3536–3548, May 2017.

N. P. W. Strachan and D. Jovcic. Stability of a variable-speed permanent magnet wind generator with weak AC grids. *IEEE Trans. Power Del.*, 25(4):2779–2788, Oct. 2010.

K. J. Åström and B. Wittenmark. *Computer-Controlled Systems: Theory and Design*. Prentice Hall, Upper Saddle River, NJ, USA, 3rd edition, 1997.

M. Su, B. Cheng, Y. Sun, Z. Tang, B. Guo, Y. Yang, F. Blaabjerg, and H. Wang. Single-sensor control of LCL-filtered grid-connected inverters. *IEEE Access*, 7: 38481–38494, 2019.

Y. Tang, P. C. Loh, P. Wang, F. H. Choo, F. Gao, and F. Blaabjerg. Generalized design of high performance shunt active power filter with output LCL filter. *IEEE Trans. Ind. Electron.*, 59(3):1443–1452, Mar. 2012.

R. Teodorescu, M. Liserre, and P. Rodriguez. *Grid Converters for Photovoltaic and Wind Power Systems*. John Wiley & Sons, Hoboken, NJ, USA, 2011.

Thuy Vi Tran, Seung-Jin Yoon, and Kyeong-Hwa Kim. An LQR-based controller design for an LCL-filtered grid-connected inverter in discrete-time state-space under distorted grid environment. *Energies*, 11(8):2062, 2018.

R. Turner, S. Walton, and R. Duke. Robust high-performance inverter control using discrete direct-design pole placement. *IEEE Trans. Ind. Electron.*, 58(1): 348–357, Jan. 2011.

J. Wang, J. D. Yan, L. Jiang, and J. Zou. Delay-dependent stability of single-loop controlled grid-connected inverters with LCL filters. *IEEE Trans. Power Electron.*, 31(1):743–757, Jan. 2016a.

X. Wang, F. Blaabjerg, and P. C. Loh. Grid-current-feedback active damping for LCL resonance in grid-connected voltage-source converters. *IEEE Trans. Power Electron.*, 31(1):213–223, Jan. 2016b.

E. Wu and P. W. Lehn. Digital current control of a voltage source converter with active damping of LCL resonance. *IEEE Trans. Power Electron.*, 21(5): 1364–1373, Sep. 2006.

G. Wu, J. Liang, X. Zhou, Y. Li, A. Egea-Alvarez, G. Li, H. Peng, and X. Zhang. Analysis and design of vector control for VSC-HVDC connected to weak grids. *CSEE Journal of Power and Energy Systems*, 3(2):115–124, Jun. 2017.

H. Wu and X. Wang. Design-oriented transient stability analysis of grid-connected converters with power synchronization control. *IEEE Trans. Ind. Electron.*, 66 (8):6473–6482, Aug. 2019.

B. Xie, M. Mao, L. Zhou, Y. Wan, and G. Hao. Systematic design of linear quadratic regulator for digitally controlled grid-connected inverters. *IET Power Electron.*, 13(3):557–567, 2020.

Z. Xin, X. Wang, P. C. Loh, and F. Blaabjerg. Grid-current-feedback control for LCL-filtered grid converters with enhanced stability. *IEEE Trans. Power Electron.*, 32(4):3216–3228, Apr. 2017.

M. Xue, Y. Zhang, Y. Kang, Y. Yi, S. Li, and F. Liu. Full feedforward of grid voltage for discrete state feedback controlled grid-connected inverter with LCL filter. *IEEE Trans. Power Electron.*, 27(10):4234–4247, Oct. 2012.

A. Yazdani and R. Iravani. *Voltage-Sourced Converters in Power Systems: Modeling, Control, and Applications*. John Wiley & Sons, 2010.

A. G. Yepes, A. Vidal, O. López, and J. Doval-Gandoy. Evaluation of techniques for cross-coupling decoupling between orthogonal axes in double synchronous reference frame current control. *IEEE Trans. Ind. Electron.*, 61(7):3527–3531, Jul. 2014.

Yongsug Suh and T. A. Lipo. Control scheme in hybrid synchronous stationary frame for PWM AC/DC converter under generalized unbalanced operating conditions. *IEEE Trans. Ind. Appl.*, 42(3):825–835, May 2006.

L. Zhang. *Modeling and Control of VSC-HVDC Links Connected to Weak AC Systems*. PhD thesis, School of Electrical Engineering, KTH Royal Institute of Technology, 2010.

L. Zhang, L. Harnefors, and H. P. Nee. Power-synchronization control of grid-connected voltage-source converters. *IEEE Trans. Power Syst.*, 25(2):809–820, May 2010.

L. Zhang, L. Harnefors, and H. P. Nee. Interconnection of two very weak AC systems by VSC-HVDC links using power-synchronization control. *IEEE Trans. Power Syst.*, 26(1):344–355, Feb. 2011a.

L. Zhang, L. Harnefors, and H. P. Nee. Modeling and control of VSC-HVDC links connected to island systems. *IEEE Trans. Power Syst.*, 26(2):783–793, May 2011b.

J. Z. Zhou and A. M. Gole. VSC transmission limitations imposed by AC system strength and AC impedance characteristics. In *Proc. 10th IET Int. Conf. AC DC Power Trans. (ACDC)*, pages 1–6, Dec. 2012.

J. Z. Zhou, H. Ding, S. Fan, Y. Zhang, and A. M. Gole. Impact of short-circuit ratio and phase-locked-loop parameters on the small-signal behavior of a VSC-HVDC converter. *IEEE Trans. Power Del.*, 29(5):2287–2296, Oct. 2014.

D. N. Zmood and D. G. Holmes. Stationary frame current regulation of PWM inverters with zero steady-state error. *IEEE Trans. Power Electron.*, 18(3): 814–822, May 2003.

D. N. Zmood, D. G. Holmes, and G. H. Bode. Frequency-domain analysis of three-phase linear current regulators. *IEEE Trans. Ind. Appl.*, 37(2):601–610, Mar./Apr. 2001.

C. Zou, B. Liu, S. Duan, and R. Li. Influence of delay on system stability and delay optimization of grid-connected inverters with LCL filter. *IEEE Trans. Ind. Informat.*, 10(3):1775–1784, Aug. 2014.

Aalto-DD 71/2021

ISBN 978-952-64-0386-1 (printed)
ISBN 978-952-64-0387-8 (pdf)
ISSN 1799-4934 (printed)
ISSN 1799-4942 (pdf)

Aalto University
School of Electrical Engineering
Department of Electrical Engineering and Automation
www.aalto.fi

BUSINESS + ECONOMY

ART + DESIGN + ARCHITECTURE

SCIENCE + TECHNOLOGY

CROSSOVER

DOCTORAL DISSERTATIONS